Photonic Band Theory of Moiré Crystals: A Two-Scale Approach

Rene-Marcel Lehner, Apl. Prof. Dr. Doris Reiter
TU Dortmund University, Condensed Matter Theory
rene-marcel.lehner@tu-dortmund.de, doris.reiter@tu-dortmund.de

September 2, 2026

Abstract

Twisting two photonic crystals against each other produces a moiré lattice whose period far exceeds that of the crystals it is built from; at generic angles the bilayer is incommensurate, and at commensurate angles the supercell grows as the inverse square of the twist angle. We develop a multi-band envelope approximation that starts from the local Bloch modes of the twisted bilayer, parametrized by the slowly varying registry between the layers, and yields an effective Hamiltonian for both polarizations whose ingredients, band energies, velocities, Löwdin-dressed mass tensors, non-Abelian Berry connections and Born–Huang potentials, are defined on the registry torus and independent of the twist angle. We state what an eigenvalue-by-eigenvalue comparison with a supercell solver requires and carry it through. On a smooth single-valley crystal the envelope model, a plane-wave reference and a finite-difference reference agree on the moiré manifold state to below 10^{-6} in frequency with a measured convergence law, and the resummed-frame limit of the theory matches all 51 states of a declared domain on a supercell of 8911 cells within the reference's own discretization error. On a strongly coupled square bilayer the model reproduces the manifold floor within the reference error and runs at angles no supercell solver reaches. For a honeycomb Dirac crystal the registry-domain geometry is obtained in a consistent gauge, and a bandwidth scan finds no magic angle within the validity window of the theory.

Keywords: photonic crystal, moiré lattice, envelope approximation, effective Hamiltonian, Berry connection, Born–Huang potential, finite-difference frequency domain, magic angle

1 Introduction

When two periodic structures are superimposed with a small relative twist, a new pattern emerges on a scale far larger than either of the originals. In crystalline matter this moiré pattern acts on a system whose waves and spectra already carry physical meaning: Bistritzer and MacDonald predicted magic angles of twisted bilayer graphene at which the Dirac velocity is suppressed and the lowest minibands become flat [1], and their experimental confirmation [2, 3] founded twistronics. Photonic crystals are the optical analogue [4], and twisted photonic bilayers have since shown localization of light [5], magic-angle flat bands and slow light in slabs [6–8], lasing [9], topological flat bands [10], bound states in the continuum [11, 12] and cavity quantum electrodynamics [13, 14]; a review is given in [15].

Computing the spectrum of a photonic moiré crystal is hard for two reasons that compound. At a generic twist angle the bilayer is incommensurate and no unit cell exists for any periodic solver. At the commensurate angles where a supercell exists, its cell count grows as θ^{-2}, and brute-force solvers run out of memory precisely where the moiré physics is richest, below about two degrees. The descriptions in the literature are either full-wave calculations for specific geometries or reduced models tailored to one setting, such as Dirac-point physics or weak coupling; a general framework across lattices, polarizations and momenta has been missing.

This paper develops such a framework for two-dimensional photonic bilayers and validates it to the precision of the best full-Maxwell solvers. The approach is a multi-band envelope approximation in the spirit of $\boldsymbol{k}\cdot\boldsymbol{p}$ theory [16, 17]: the local Bloch modes of a two-atomic crystal, parametrized by the slowly varying registry between the layers, carry the fast physics, and a two-scale expansion yields an effective Hamiltonian for moiré-scale envelopes alone. The contributions are the following.

1. A two-scale derivation of the envelope operator for both polarizations through second order in the scale-separation parameter, with every geometric term explicit: the non-Abelian Berry connection [18, 19], the remote-band Löwdin mass tensor [20] and an ϵ^{-1}-weighted Born–Huang leakage potential [21], together with the limit the expansion converges to (Sec. 3).
2. A pipeline in which all Hamiltonian data are computed once per crystal on the registry torus and reused for every twist angle, and the finding that finite-difference references at one pixel per lattice constant reproduce the low-frequency moiré spectrum (Sec. 4).
3. A protocol for eigenvalue-by-eigenvalue comparison between an envelope model and a supercell solver, with certified state counts (Sec. 5).
4. Validation on a strongly coupled square bilayer, where the model reproduces the manifold floor within the reference's own error and is the only solver below 2°, and on a smooth single-valley crystal, where three solvers agree on every state of a declared domain within the reference's discretization error (Sec. 6).
5. Gauge-consistent registry-domain maps of the Dirac geometry of a honeycomb crystal and a bandwidth scan that finds no magic angle within the validity window of the theory (Sec. 7).

The plane-wave solver that feeds the pipeline, Blaze2D, is described in a companion paper [22].

2 Photonic Moiré Crystals and Local Periodicity

For a permittivity $\epsilon(\boldsymbol{x})$ that is periodic in the plane and invariant along z, Maxwell's equations decouple into two scalar polarizations, both generalized Hermitian eigenproblems $A\psi = \lambda B\psi$ with $\lambda = \omega^2/c^2$,

$$\text{TE } (H_z): \quad -\nabla\cdot\left[\epsilon^{-1}(\boldsymbol{x})\,\nabla H_z\right] = \lambda\, H_z, \tag{1}$$

$$\text{TM } (E_z): \quad -\nabla^2 E_z = \lambda\,\epsilon(\boldsymbol{x})\, E_z, \tag{2}$$

which Bloch's theorem reduces to one primitive cell; plane-wave expansion (PWE) [23] and finite-difference frequency-domain (FDFD) discretizations [24, 25] are the standard solvers.

A photonic moiré crystal is a bilayer of two such crystals rotated by $\pm\theta/2$. The superposition modulates the local stacking with the moiré period

$$L = \frac{a}{2\sin(\theta/2)} \approx \frac{a}{\theta}, \tag{3}$$

where a is the monolayer lattice constant; a 2° twist already gives $L \approx 29a$. Exact periodicity survives only at commensurate angles, where the coincidence-site lattice defines a supercell (for the square lattice and coprime (p, q), $\theta_{pq} = 2\arctan(q/p)$ with supercell side $a\sqrt{p^2+q^2}$). The number of monolayer cells per moiré cell scales as $(L/a)^2 \approx \theta^{-2}$, about 800 at 2° and more than 3000 at 1°, and a supercell solver must resolve every one of them: at 64 pixels per lattice constant a single 2° moiré cell has 3.4×10^6 grid points, and both PWE and FDFD exceed workstation memory below 2–3°. At generic angles no supercell exists at all.

Local periodicity. At small angles every patch of the bilayer resembles a periodic crystal with a two-atom basis whose interlayer shift varies smoothly from patch to patch (Fig. 7 in the appendix). For each shift $\boldsymbol{\delta}$ we define the periodic two-atomic crystal

$$\epsilon_{\mathrm{loc}}(\boldsymbol{r};\boldsymbol{\delta}) := \epsilon_1(\boldsymbol{r}) + \epsilon_2(\boldsymbol{r}+\boldsymbol{\delta}), \tag{4}$$

periodic in the fast coordinate $\boldsymbol{r}$ on the monolayer cell; the moiré pattern enters through the registry map $\boldsymbol{\delta} = \boldsymbol{\delta}(\boldsymbol{R})$. For layers rotated by $\pm\theta/2$ the relative displacement at the physical point $\boldsymbol{x}$ is $(R_{-\theta/2} - R_{+\theta/2})\,\boldsymbol{x} = -2\sin(\theta/2)\,J\boldsymbol{x}$, with J the rotation by 90°. In units of a and in the slow coordinate $\boldsymbol{R} = \boldsymbol{x}/L$ the two small factors cancel exactly,

$$\boldsymbol{\delta}_{\mathrm{raw}}(\boldsymbol{R}) := \left(R_{-\theta/2} - R_{+\theta/2}\right)\frac{\boldsymbol{x}}{a} = -J\boldsymbol{R}, \tag{5}$$

so the registry advances by one lattice constant per moiré period and its slow gradient is the constant matrix $\partial_{\boldsymbol{R}}\boldsymbol{\delta} = -J$, with no remaining factor of the twist angle. The registry map proper is $\boldsymbol{\delta}_{\mathrm{raw}}$ reduced modulo the monolayer Bravais lattice, a map onto the registry torus, and the family $\boldsymbol{\delta} \mapsto \epsilon_{\mathrm{loc}}(\cdot\,;\boldsymbol{\delta})$ is assumed smooth enough to be differentiated.

Validity. Freezing the shift at $\boldsymbol{\delta}(\boldsymbol{R}_0)$ and tiling that crystal is accurate only as long as the true registry has not drifted appreciably over the distance a crystal needs to develop its spectral identity. A stop-band of relative width γ (gap-to-midgap ratio) forms over a Bragg penetration depth of roughly $1/\gamma$ periods [26], over which the registry drifts by θ/γ lattice constants. The quality parameter

$$\beta := \theta/\gamma \tag{6}$$

(θ in radians) is the accumulated registry mismatch at the distance where the band structure is established: for $\beta \ll 1$ the local crystal barely changes over that length, for $\beta \gtrsim 1$ the local-periodicity picture breaks down (accuracy zones in Fig. 8 of the appendix).

3 The Multi-Band Envelope Approximation

Two-scale lift. Let $\eta := a/L \ll 1$ and introduce the dimensionless coordinates $\boldsymbol{r} := \boldsymbol{x}/a$ and $\boldsymbol{R} := \boldsymbol{x}/L$. Following the two-scale method of homogenization theory [27, 28], $\boldsymbol{r}$ and $\boldsymbol{R}$ are promoted to independent variables: a lifted quantity $\Phi(\boldsymbol{r},\boldsymbol{R})$ has the physical realization $\Phi^{\eta}(\boldsymbol{x}) := \Phi(\boldsymbol{x}/a, \boldsymbol{x}/L)$ on the diagonal, and the chain rule $\nabla_{\boldsymbol{x}} = a^{-1}(\nabla_{\boldsymbol{r}} + \eta\nabla_{\boldsymbol{R}})$ is exact there. The lifted permittivity is $\epsilon(\boldsymbol{r},\boldsymbol{R}) := \epsilon_{\mathrm{loc}}(\boldsymbol{r};\boldsymbol{\delta}(\boldsymbol{R}))$. Locking the fast coordinate to the first layer, $\boldsymbol{r}_1 := R_{+\theta/2}\boldsymbol{x}/a$, represents the true bilayer exactly,

$$\epsilon_{\mathrm{bilayer}}(\boldsymbol{x}) = \epsilon_1(\boldsymbol{r}_1) + \epsilon_2(\boldsymbol{r}_1 - J\boldsymbol{R}), \tag{7}$$

with the registry map Eq. (5) entering exactly; the diagonal restriction of the lifted proxy differs from it only by a dilation of the fast frame by $\cos(\theta/2) = 1 - \eta^2/8 + O(\eta^4)$, absorbed into the local band data. Since $\boldsymbol{R}$ enters ϵ only through the registry map, slow derivatives act with the constant Jacobian $\partial_{R_j}\boldsymbol{\delta} = -J\boldsymbol{e}_j$.

Local Bloch problems and the ansatz. For each fixed $\boldsymbol{R}$ the fast variable sees an ordinary periodic crystal. For TE,

$$-D_{\boldsymbol{r}}(\boldsymbol{k})\cdot\left[\epsilon^{-1}(\boldsymbol{r},\boldsymbol{R})\,D_{\boldsymbol{r}}(\boldsymbol{k})\right]u_{n\boldsymbol{k}}(\boldsymbol{r};\boldsymbol{R}) = \lambda_n(\boldsymbol{R},\boldsymbol{k})\,u_{n\boldsymbol{k}}(\boldsymbol{r};\boldsymbol{R}), \qquad D_{\boldsymbol{r}}(\boldsymbol{k}) := \nabla_{\boldsymbol{r}} + \mathrm{i}\boldsymbol{k}, \tag{8}$$

with periodic boundary conditions in $\boldsymbol{r}$ and parametric dependence on $\boldsymbol{R}$. The moiré Brillouin zone is smaller than the monolayer zone by the factor η, so a moiré Bloch momentum $\boldsymbol{q}$ displaces

the monolayer momentum only slightly from a chosen carrier $\boldsymbol{k}_0$. The ansatz attaches slow envelopes to N retained local Bloch states at the carrier and factors both Bloch phases,

$$H_{\boldsymbol{k}_0\boldsymbol{q}}(\boldsymbol{r},\boldsymbol{R}) \approx \mathrm{e}^{\mathrm{i}\boldsymbol{k}_0\cdot\boldsymbol{r}}\,\mathrm{e}^{\mathrm{i}\boldsymbol{q}\cdot\boldsymbol{R}}\,\psi_{\boldsymbol{q}}(\boldsymbol{r},\boldsymbol{R}), \qquad \psi_{\boldsymbol{q}} := \sum_{n=1}^{N} f_{n\boldsymbol{q}}(\boldsymbol{R})\,u_{n\boldsymbol{k}_0}(\boldsymbol{r};\boldsymbol{R}), \tag{9}$$

where the moiré-periodic envelopes $f_{n\boldsymbol{q}}$ form the vector $\boldsymbol{f}_{\boldsymbol{q}}$. The approximation sign is the truncation to N bands; everything that follows is exact algebra. With the fast-cell inner product $\langle g,\,h\rangle_\Omega := |\Omega|^{-1}\int_\Omega g^* h\,\mathrm{d}\boldsymbol{r}$ the retained states are orthonormal, $\langle u_m,\,u_n\rangle_\Omega = \delta_{mn}$, and slow amplitudes are extracted by projection onto them.

Order expansion. Inserting Eq. (9) into the lifted TE master equation, multiplied by a^2 so that λ is dimensionless, and pushing the gradients through the phases with $D_{\boldsymbol{r}} := \nabla_{\boldsymbol{r}} + \mathrm{i}\boldsymbol{k}_0$ and $D_{\boldsymbol{R}} := \nabla_{\boldsymbol{R}} + \mathrm{i}\boldsymbol{q}$ yields an operator on the periodic core, $\mathcal{L}_{\mathrm{TE,eff}}\,\psi_{\boldsymbol{q}} = \lambda\,\psi_{\boldsymbol{q}}$, that separates in powers of η:

$$\mathcal{L}_{\mathrm{TE,eff}} = \mathcal{L}^{(0)} + \eta\,\mathcal{L}^{(1)} + \eta^2\mathcal{L}^{(2)}, \qquad \begin{aligned} \mathcal{L}^{(0)} &:= -D_{\boldsymbol{r}}\cdot\big(\epsilon^{-1}D_{\boldsymbol{r}}\big),\\ \mathcal{L}^{(1)} &:= -D_{\boldsymbol{r}}\cdot\big(\epsilon^{-1}D_{\boldsymbol{R}}\big) - D_{\boldsymbol{R}}\cdot\big(\epsilon^{-1}D_{\boldsymbol{r}}\big),\\ \mathcal{L}^{(2)} &:= -D_{\boldsymbol{R}}\cdot\big(\epsilon^{-1}D_{\boldsymbol{R}}\big). \end{aligned} \tag{10}$$

The slow derivative acts on everything to its right, including the $\boldsymbol{R}$-dependence of ϵ^{-1} through the registry map, so the slow-coefficient terms are built in. From here on $u_n := u_{n\boldsymbol{k}_0}(\boldsymbol{r};\boldsymbol{R})$, $\lambda_n := \lambda_n(\boldsymbol{R};\boldsymbol{k}_0)$, repeated Cartesian indices $i,j \in \{x,y\}$ are summed, and $\boldsymbol{q}$ enters only through $D_{R_i} = \partial_{R_i} + \mathrm{i}q_i$.

At zeroth order the local eigenproblem gives the diagonal band-energy matrix $\Lambda_{mn}(\boldsymbol{R};\boldsymbol{k}_0) := \lambda_n\delta_{mn}$. At first order the terms in which the slow derivative acts on the envelope are organized by the local velocity operator, the $\boldsymbol{k}$-derivative of the Bloch operator $\mathcal{L}_0(\boldsymbol{R},\boldsymbol{k}) := -D_{\boldsymbol{r}}(\boldsymbol{k})\cdot(\epsilon^{-1}D_{\boldsymbol{r}}(\boldsymbol{k}))$ at the carrier,

$$\mathcal{V}_i := \partial_{k_i}\mathcal{L}_0(\boldsymbol{R},\boldsymbol{k})\big|_{\boldsymbol{k}=\boldsymbol{k}_0}, \qquad \mathcal{V}_i\phi = -\mathrm{i}\big[D_{r_i}(\epsilon^{-1}\phi) + \epsilon^{-1}D_{r_i}\phi\big], \qquad v^{(i)}_{mn} := \langle u_m,\,\mathcal{V}_i u_n\rangle_\Omega\,, \tag{11}$$

while the terms in which it acts on u_n or on ϵ^{-1} form an exact remainder. At second order the direct projection produces the ϵ^{-1}-weighted metric $G_{mn} := \big\langle u_m,\,\epsilon^{-1}u_n\big\rangle_\Omega$, a one-derivative coefficient and a scalar; these direct coefficients are gauge-dependent intermediates.

Frame geometry. Collect the retained states columnwise in $U(\boldsymbol{R})$ with $U^\dagger U = \mathbb{1}_N$, and let $P := UU^\dagger$ and $Q := 1 - P$ project onto the retained manifold and the remote complement (a globally smooth frame over the moiré cell is assumed). Because U is orthonormal, its slow derivative splits into an in-manifold rotation and a leakage into Q,

$$A_i := \mathrm{i}\,U^\dagger\partial_{R_i}U, \qquad \partial_{R_i}U = -\mathrm{i}\,UA_i + \Xi_i, \qquad \Xi_i := Q\,\partial_{R_i}U, \tag{12}$$

where A_i is the Hermitian non-Abelian Berry connection and Ξ_i the exact geometric leakage. They induce the covariant slow derivative and momentum, and an exact product rule for the ansatz,

$$\mathcal{D}_i := D_{R_i} - \mathrm{i}A_i, \qquad \Pi_i := -\mathrm{i}\,\mathcal{D}_i, \qquad D_{R_i}\big(U\boldsymbol{f}_{\boldsymbol{q}}\big) = U\mathcal{D}_i\boldsymbol{f}_{\boldsymbol{q}} + \Xi_i\boldsymbol{f}_{\boldsymbol{q}}. \tag{13}$$

Downfolding. The remote complement is not dropped. Assuming a local spectral gap $\Delta(\boldsymbol{R}) > 0$ between the retained manifold and the rest, uniformly over the registry torus, the periodic core is $\Psi = U\boldsymbol{f}_{\boldsymbol{q}} + \eta\chi + O(\eta^2)$ with $Q\chi = \chi$, and Löwdin partitioning [20] with the reduced resolvent $R_Q := [Q(\mathcal{L}^{(0)} - \lambda_{\mathrm{ref}})Q]^{-1}$ gives the closed operator through $O(\eta^2)$,

$$\mathcal{H}_{\mathrm{eff}} = \Lambda + \eta\,U^\dagger\mathcal{L}^{(1)}U + \eta^2\Big[U^\dagger\mathcal{L}^{(2)}U - U^\dagger\mathcal{L}^{(1)}Q\,R_Q\,Q\mathcal{L}^{(1)}U\Big]. \tag{14}$$

Evaluated order by order, the first order is the Berry-covariant drift

$$U^\dagger \mathcal{L}^{(1)} U = \tfrac{1}{2}\big(v^{(i)}\Pi_i + \Pi_i v^{(i)}\big) + U^{(1)}_{\rm rem}, \qquad U^{(1)}_{\rm rem} = \Xi^{(1)}_{\rm sc} + \tfrac{\mathrm{i}}{2}\,\partial_{R_i} v^{(i)} + \tfrac{1}{2}\big[A_i,\, v^{(i)}\big], \tag{15}$$

where $\Xi^{(1)}_{\rm sc}$ collects the leakage and slow-dielectric terms (Appendix B). The Berry connection enters once, through Π_i; the commutator is what remains when the symmetrized product is expanded, and it must not be counted a second time. At second order the direct metric and the remote-band excursion combine, after the Hermitian Löwdin symmetrization that replaces $\lambda_{\rm ref}$ by the retained band energies, into the inverse mass tensor

$$\big(M^{-1}_{ij}\big)_{mn} := 2\,\delta_{ij}\,G_{mn} + \sum_{\ell\notin P}\left[\frac{v^{(i)}_{m\ell}\,v^{(j)}_{\ell n}}{\lambda_n-\lambda_\ell} + \frac{v^{(j)}_{m\ell}\,v^{(i)}_{\ell n}}{\lambda_m-\lambda_\ell}\right]. \tag{16}$$

The remaining direct second-order terms are stated most cleanly in flux form: by Eq. (13) the slow flux of the ansatz is $U\mathcal{D}_i \boldsymbol{f_q} + \Xi_i \boldsymbol{f_q}$, and projecting its ϵ^{-1}-weighted square onto the frame gives

$$\mathcal{H}^{(2)}_{\rm dir} = -\mathcal{D}_i\big(G\,\mathcal{D}_i + K_i\big) + K_i^\dagger \mathcal{D}_i + U_{\rm BH}, \qquad K_i := U^\dagger \epsilon^{-1}\Xi_i, \qquad U_{\rm BH} := \Xi_i^\dagger\,\epsilon^{-1}\,\Xi_i, \tag{17}$$

with the slow derivatives acting on everything to their right. The last term is the exact Born–Huang leakage penalty [21], weighted by ϵ^{-1}; the unweighted form $\Xi_i^\dagger\Xi_i$ is a modelling simplification, not an identity. The remote-band excursion is the manifestly Hermitian $-S^\dagger R_Q S$ with $S = \mathcal{T}_i\mathcal{D}_i + \mathcal{R}$ (Appendix B); its kinetic part is the Löwdin sum in Eq. (16), and its one-derivative and scalar parts join the K terms and $U_{\rm BH}$ in the second-order remainder $U^{(2)}_{\rm rem}$. Collecting everything,

$$\boxed{\mathcal{H}_{\rm eff} = \Lambda + \eta\left[\tfrac{1}{2}\big(v^{(i)}\Pi_i + \Pi_i v^{(i)}\big) + U^{(1)}_{\rm rem}\right] + \eta^2\left[\tfrac{1}{2}\,\Pi_i\,M^{-1}_{ij}\,\Pi_j + U^{(2)}_{\rm rem}\right] + O(\eta^3),} \tag{18}$$

acting on the moiré-periodic envelope, $\mathcal{H}_{\rm eff}\boldsymbol{f_q} = \lambda \boldsymbol{f_q}$. Because Λ is kept diagonal and the Löwdin denominators carry band labels, the admissible frame changes $U \to UW(\boldsymbol{R})$ are phases of individual states, permutations and rotations inside degenerate blocks. The complete operator with every term written out is displayed for both polarizations in Appendix A.

TM polarization. The TM problem carries ϵ as a weight. Setting $\rho := \epsilon^{-1/2}$ and $\tilde{E} := \epsilon^{1/2}E$ turns the lifted generalized problem into the standard Hermitian one

$$\tilde{\mathcal{H}}^{\eta}_{\rm TM} = -\rho\,\big(D_{\boldsymbol{r}} + \eta D_{\boldsymbol{R}}\big)^2\rho, \tag{19}$$

whose orders carry gradients of ϵ as drifts and scalar potentials. Projecting onto the hermitized Bloch states $\tilde{u}_n := \epsilon^{1/2}u^{\rm TM}_n$ and downfolding as before gives an operator of exactly the form Eq. (18), with the velocity $\tilde{\mathcal{V}}_i\phi := -2\mathrm{i}\,\rho D_{r_i}(\rho\phi)$, the metric $\tilde{G}_{mn} = \big\langle \tilde{u}_m,\, \epsilon^{-1}\tilde{u}_n\big\rangle_\Omega$ and, in the flux form, the leakage flux

$$Y_i := \rho\,\tilde{\Xi}_i + (\partial_{R_i}\rho)\,\tilde{U}, \qquad \tilde{\Xi}_i := Q\,\partial_{R_i}\tilde{U}, \qquad \tilde{U}_{\rm BH} = Y_i^\dagger Y_i, \tag{20}$$

which contains, besides the ϵ^{-1}-weighted frame leakage, the slow variation of the hermitizing factor itself, a term with no TE analogue.

The resummed limit. Every term generated by slow derivatives acting on a frame frozen at $\boldsymbol{k}_0$ has one origin: an envelope with moiré momentum $\boldsymbol{q}$ represents a Bloch state at the monolayer momentum $\boldsymbol{k}_0 + \eta\boldsymbol{q}$, and the local band data are analytic in $\boldsymbol{k}$: the velocity, the mass tensor (the sum rule of $\boldsymbol{k}\cdot\boldsymbol{p}$ theory) and the frame terms are the Taylor coefficients of the local band data

in $\eta\boldsymbol{q}$. Nothing forces the frame to stay frozen: for an envelope periodic on the moiré lattice the admissible momenta form the discrete set $\boldsymbol{k}_p = \boldsymbol{k}_0 + \eta\boldsymbol{G}_p$ over the moiré reciprocal lattice, and using the exact local Bloch state at each of them sums all orders at once. For the TM pencil with one retained band of the registry-averaged crystal (for a weak second layer, the first layer alone) distinct harmonics are distinct momentum cosets, the kinetic block is diagonal, and only the Fourier harmonics $c_{\boldsymbol{h}}$ of the second layer couple harmonics:

$$\operatorname{diag}\big(\lambda_1(\boldsymbol{k}_p)\big)\,\boldsymbol{c} = \lambda\,\big(\mathbb{1} + V\big)\,\boldsymbol{c}, \qquad V_{pp'} = c_{\boldsymbol{h}}\,\Big\langle u_1(\boldsymbol{k}_p),\, \mathrm{e}^{\mathrm{i}\boldsymbol{h}\cdot\boldsymbol{r}}\, u_1(\boldsymbol{k}_{p'})\Big\rangle_{\Omega} \quad \text{for} \quad \boldsymbol{G}_p - \boldsymbol{G}_{p'} = W^T\boldsymbol{h}, \tag{21}$$

and $V_{pp'} = 0$ otherwise, where W is the integer matrix that turns a monolayer harmonic of the second layer into a moiré harmonic, the reciprocal-space image of $\boldsymbol{\delta} = -J\boldsymbol{R}$ on a commensurate cell. Exact band data enter on the left, the interlayer coupling is a nearest-neighbour hopping over moiré harmonics on the right, no supercell object appears anywhere, and the cost is one monolayer solve per harmonic. We call this the resummed-frame model; its remaining error is the registry dressing of the frames themselves, second order in the interlayer coupling.

4 From the Hamiltonian to Numbers

The pipeline splits into two phases. *Phase 1* is the registry sweep: for every point $\boldsymbol{\delta}_j$ of a grid covering one period of the registry torus, the local two-atomic crystal $\epsilon_{\mathrm{loc}}(\boldsymbol{r};\boldsymbol{\delta}_j)$ is diagonalized at the carrier $\boldsymbol{k}_0$ with full eigenvector extraction, and the ingredients of Eq. (18) are assembled from the retained and remote bands. Because the registry map does not involve the twist angle, the tabulation is twist-invariant and serves every angle. The sweep needs thousands of solves with explicit operator matrices and cross-subspace couplings, for which the plane-wave eigensolver Blaze2D was written [22, 29, 30]. *Phase 2* introduces the angle: η scales the slow derivatives, the registry data are mapped onto a moiré-scale grid, $\mathcal{D}_i$ is discretized with Bloch-periodic finite differences, and the sparse Hermitian matrix is solved by shift-invert Lanczos around a target inside the spectral range of Λ. The geometric terms are not small corrections: on square rods at M and hexagonal holes at K the Born–Huang term outweighs the kinetic term in every configuration and exceeds the local potential itself in three of four (Fig. 9 in the appendix).

Reference solvers. Independent references were built from MPB [23] and from an FDFD eigensolver. In fractional supercell coordinates with the moiré lattice matrix $B = [\boldsymbol{L}_1 \,|\, \boldsymbol{L}_2]$ and metric $g^{\alpha\beta} = (B^{-1}B^{-T})_{\alpha\beta}$, the TE operator is assembled from forward differences D^+_α with Bloch-periodic boundaries,

$$L_{\mathrm{TE}} = \sum_{\alpha\beta} g^{\alpha\beta}\,\big(D^+_\alpha\big)^\dagger\,\epsilon^{-1}\,D^+_\beta, \qquad L_{\mathrm{TE}}\,\boldsymbol{u} = \lambda\,\boldsymbol{u}, \tag{22}$$

with ϵ^{-1} a diagonal matrix of pixel averages; the sparse operator is factored once with CHOLMOD [31] and shift-inverted. On a monolayer the two solvers agree to 10^{-4} (TM) and 10^{-3} (TE) in relative frequency.

The decisive property is shown in Fig. 10 in the appendix: on a $(38, 1)$ square supercell at $3°$ (1445 cells, 50 TM modes at Γ), FDFD at one pixel per lattice constant already traces the lower half of the MPB spectrum, and the intra-method error drops by four orders of magnitude between 1 and 16 pixels. One pixel per lattice constant means one number per unit cell: the rods are averaged away entirely, and what survives is the slowly varying moiré-scale modulation of ϵ^{-1}, the same scale separation the envelope theory formalizes; the 1 px/a mode profiles reproduce the moiré-scale envelopes of the 32 px/a MPB modes. Since memory scales as $R^2 N_{\mathrm{cells}}$, coarse FDFD provides a cheap reference exactly where the envelope theory is most accurate.

5 What a Faithful Comparison Requires

Do the envelope model and a supercell solver produce the same eigenvalues? Before a single number is compared, the comparison must satisfy five requirements, each established after a comparison had failed for the lack of it.

Spectral isolation everywhere. The retained manifold must be separated from every other band at every registry and across the whole monolayer zone, not only at the carrier: a *registry-common gap*, the maximum of band n over all registries and momenta lying below the minimum of band $n+1$. Without it the target states sit inside the folded continuum of a neighbouring band at some registry, hybridize with it and dissolve into resonances, and no method can match them one by one.

Certified counts. Both sides must enumerate every state of the window, and the counts must agree before any residual is read. For a plane-wave or FDFD pencil $K - \lambda S$ the number of eigenvalues below λ follows exactly from the inertia of its LDL^T factorization (Sylvester's law); the envelope model's count is fixed by construction once its trial space is built on a declared set of moiré harmonics.

Sorted, index-aligned matching. No assignment algorithm: any two ladders of comparable density can be matched to within a level spacing, so an optimal assignment proves nothing.

Extrapolated references. An FDFD ladder at one resolution is not a reference at the 10^{-6} level. Each state is extrapolated in the grid spacing from three resolutions with a fitted order and an uncertainty; the plane-wave reference is converged in its cutoff and certified by residuals. Two references that agree define the floor below which no claim is made.

Symmetry bookkeeping. The $(m, 1)$ cell is centred, $(\boldsymbol{L}_1 + \boldsymbol{L}_2)/2$ being a lattice vector of both layers, so every level at the folded X momentum is an exact doublet of that hidden translation, and the two monolayer valleys X and X' fold onto the same supercell momentum, related by the four-fold rotation. A comparison that does not resolve these sectors compares mixtures.

Finally the discrete operator must be sound. Four pitfalls were invisible in aggregate comparisons and fatal in exact ones: a kinetic term assembled as the square of a first-derivative stencil, whose symbol vanishes at the Nyquist momentum and supports four interleaved copies of the spectrum; a remote-band term assembled as LR_QR' with $R' \neq L^\dagger$, which injects a spurious attractive potential; registry derivatives of discretized rod boundaries entering as grid-divergent fields; and a single-precision eigensolve. Every number below was produced with an operator free of all four, or with the resummed-frame model Eq. (21), which contains none of these terms.

6 Results

6.1 The strongly coupled square bilayer

The first crystal is a TM square bilayer of dielectric rods, $\epsilon = 8.9$, with the manifold of band 1 at the carrier X. Equal rods of radius $0.20a$ in both layers fail the first requirement: as the registry sweeps the torus the local crystal morphs from aligned to checkerboard, band 0 at other registries overlaps the band-1 window at X, and the manifold dissolves; at 2° every FDFD state in the window carries an X-star Fourier weight below two percent (Fig. 11 in the appendix). A weak second layer of half the radius, $r_1 = 0.20a$ and $r_2 = 0.10a$, keeps the gap of the first layer open at every registry, and band 1 at X becomes an isolated manifold with a headroom of 0.12 to band 2.

It is still a hard case, and the reason can be read off monolayer data: band 1 at X spans $\lambda \in [5.316, 7.612]$ over the registry torus, a potential $V = 2.30$, while the gaps to bands 0 and 2 are 2.31 and 4.19. The moiré potential is as deep as the band gap that isolates it, $V/\Delta \approx 1$, and at 2° the kinetic quantum $\frac{1}{2}M^{-1}(2\pi\eta)^2 \approx 0.024$ is a hundred times smaller. The manifold

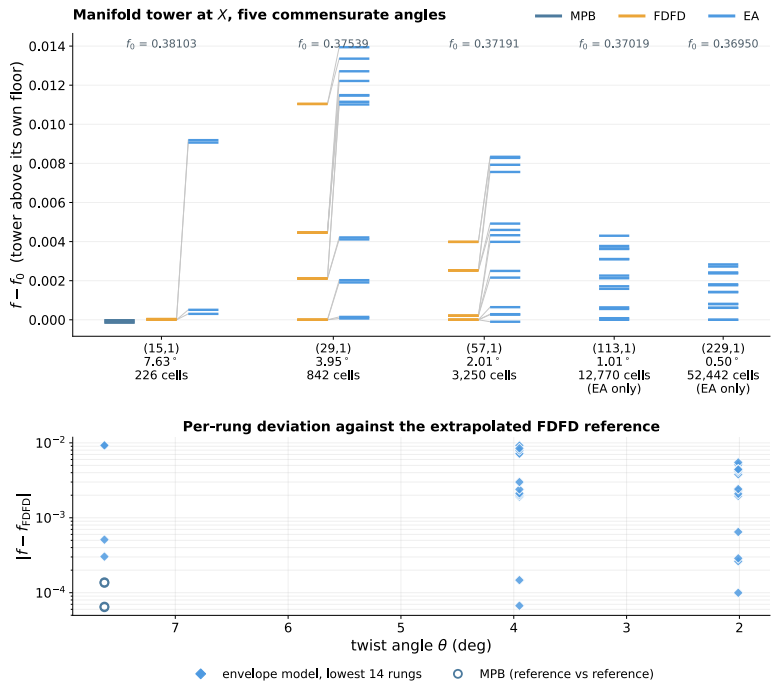

Figure 1: The square bilayer angle by angle (TM, $r_1 = 0.20a$, $r_2 = 0.10a$, $\epsilon = 8.9$, carrier X, band 1). *Top*: the lowest fourteen rungs of the manifold tower in MPB (steel blue), extrapolated FDFD (orange) and the resummed-frame envelope model (sky blue), each group referred to its own floor f_0; grey lines join equal indices. At 1.01° and 0.50° only the envelope model exists. *Bottom*: per-rung deviation against the extrapolated FDFD reference where one exists; open circles are MPB against FDFD, the reference-versus-reference floor.

states are pocket-bound, the supercell ground state sitting 0.42 above the registry minimum, and the tower above the floor is shaped by the wells rather than by the band dispersion. This strong-coupling wall is computable a priori.

Figure 1 shows the manifold tower at five commensurate angles in every solver that reaches the angle. All solvers consume the identical analytic dielectric, converged in the plane-wave cutoff to 2×10^{-7} in λ. FDFD references at 7.63°, 3.95° and 2.01° are inertia-certified and Richardson-extrapolated with a fitted order of 2.05; MPB at resolution 24 differs from them by 1.4×10^{-4} in frequency, its own un-extrapolated discretization error. The envelope model is the registry-adapted resummed-frame model Eq. (21) with a 6×6 envelope box. The floor is reproduced: the model places the manifold bottom at 3.0×10^{-4}, 6.7×10^{-5} and 1.0×10^{-4} in frequency from the extrapolated FDFD value at the three reference angles, inside MPB's own error at each. The tower is not: at 2.01° the fourteen lowest envelope rungs span 0.0084 where the FDFD rungs span 0.0040, and a larger envelope box does not close the gap. The cause is symmetry. The FDFD tower consists of four-fold degenerate quartets, the $X \oplus X'$ structure of the centred cell; the trial set was closed under the four-fold rotation, but the parallel-transport gauge that smooths the registry-adapted frames picks a direction, so the trial span is not covariant and the quartets split. A point-group-covariant gauge for the adapted frames is the bounded next step.

The ladder also shows where the envelope model stands as a solver. FDFD took 13 s, 65 s and 3221 s at the three reference angles, and the 1.01° cell did not fit in memory; the envelope model's cost shrinks with the angle, because pocket-bound envelopes have a fixed width in moiré-harmonic units, and the 0.50° case, 52 442 moiré cells, took 533 s. The certified FDFD towers also settle the bandwidth scaling on this crystal: they span 0.0040 at 2.01° and 0.011 at 3.95°, a ratio of 2.7 where θ^2 predicts 3.9; the quadratic law belongs to kinetic-dominated towers.

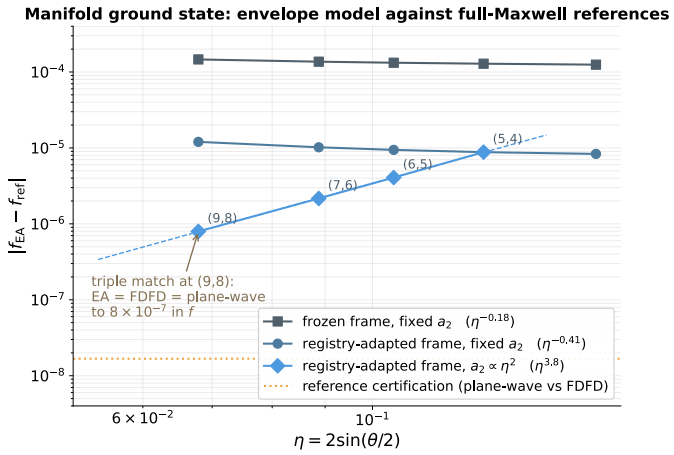

Figure 2: Deviation of the envelope model's manifold ground state from the certified plane-wave reference on the smooth single-valley crystal, against $\eta = 2\sin(\theta/2)$: the frozen-frame single-band model at fixed material (grey), the registry-adapted single-band model at fixed material (steel blue) and the registry-adapted model on the uniform family $a_2 \propto \eta^2$ (sky blue, with the fitted power law). The dotted line is the agreement between the two references.

6.2 Where the approximation is exact

The requirements of Sec. 5 translate into a design brief: an isolated manifold with a registry-common gap, a weak-to-moderate modulation, a twist angle at which a supercell is still brute-force solvable, a smooth band-limited dielectric so that every solver consumes identical analytic coefficients and the registry derivatives are finite, and few enough unknowns that every solver can be over-converged. The candidate is a hexagonal lattice with $\epsilon_0 = 9$, a host layer of three Fourier stars with amplitudes 2.95, 2.25 and 2.60, detuned so that the three M points are inequivalent, and a weak second layer with one star of amplitude $a_2 = 0.12$. Band 1 of the registry-averaged crystal has its minimum at M_2, which is time-reversal invariant and has no valley partner; the next M point lies 0.011 higher, the window has depth $V = 0.023$, a registry-common gap extends 0.148 above the floor, and band 2 sits 0.611 higher still. The family $(m, m-1)$ from $(4,3)$ to $(9,8)$ spans 37 to 217 primitive cells. A hermitized plane-wave collocation operator with certified residuals below 8×10^{-12} and the FDFD leg at 16, 24 and 32 px/a agree to 1.7×10^{-8} in frequency across the family, the floor of everything that follows.

Figure 2 separates what the frame does from what the family does. A frozen frame, one Bloch function taken at the carrier and used at every registry, sits on a flat floor of 2.0 to 2.4×10^{-3} in λ with exponent $\eta^{-0.18}$: it cannot follow the rotation of the Bloch state with the registry, and the error is second order in the coupling and independent of the angle. The registry-adapted frame, in which the local Bloch function $u_1(\boldsymbol{\delta}(\boldsymbol{R}))$ enters the trial space at every slow point and the slow derivative differentiates through it, so that every frame-derivative, Berry and leakage term enters mechanically, is fifteen times better at fixed material but still not asymptotic, $\eta^{-0.41}$, because at fixed material V/E_{kin} grows as η^{-2}. On the uniform family $a_2 \propto \eta^2$, which keeps V/E_{kin} fixed, the adapted model converges as $\eta^{3.79}$ to 1.28×10^{-5} in λ at $(9,8)$, where the three solvers agree on the manifold state:

$$|f_{\mathrm{EA}} - f_{\mathrm{PWE}}| = 7.9\times10^{-7}, \qquad |f_{\mathrm{EA}} - f_{\mathrm{FDFD}}| = 8.1\times10^{-7}, \qquad |f_{\mathrm{PWE}} - f_{\mathrm{FDFD}}| = 1.7\times10^{-8}. \tag{23}$$

A single matched state is not a validation. The commensurate dielectric of finite-Fourier layers has an exact thirteen-term supercell Fourier series, so the TM pencil $K\boldsymbol{u} = \lambda S\boldsymbol{u}$ is sparse and the inertia of $K - \lambda S$ certifies every census. At $(18,17)$, 919 cells, the two references agree on all 47 states of the gap window to between 3 and 8×10^{-8} in frequency; at $(32,31)$, 2977 cells, on all 85. A per-state diagnosis against such a tower explains every miss and every extra level of the

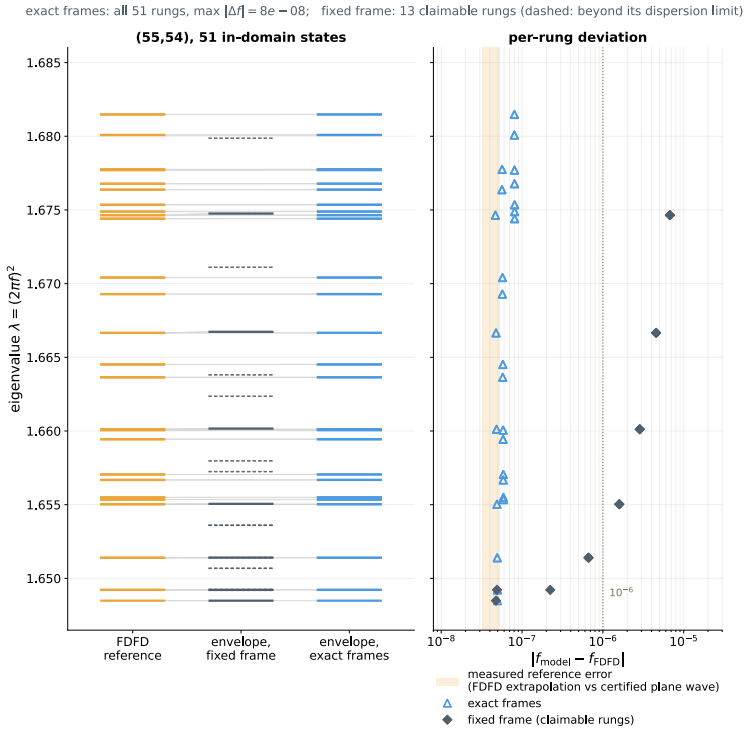

Figure 3: Every state of the declared single-valley domain at $(55, 54)$, 8911 cells, 0.607°. *Left*: the FDFD reference, the fixed-frame envelope model (dashed where beyond its a-priori dispersion limit) and the exact-frame single-band model; matched rungs joined. *Right*: per-rung deviation of both models against the measured reference error, the difference between the FDFD extrapolation and the certified plane-wave pencil calibrated on the 21 in-domain states at $(32, 31)$.

frozen-frame envelope model: missed states belong to another valley basin or lie above the ceiling at which states of the M_3 basin legitimately enter the sector (0.0355 above M_2), and extra levels carry harmonics outside the model's domain (Fig. 13 in the appendix). The sharper finding concerns direction: the fixed-frame envelope surface is nearly isotropic while the true band is anisotropic by ten to one, light-direction rungs match at 3.7×10^{-7} while heavy-direction rungs err by 1.5×10^{-5} and more, and the dispersion gap between the two surfaces, computable from the monolayer alone, predicts the error rung by rung before any supercell is solved. Everything can therefore be declared before any supercell is solved: the domain (harmonics in the M_2 basin at or below the M_3 floor), the models built on it, the certified censuses, and the matching.

Figure 3 applies this at $(55, 54)$, 8911 cells, $\theta = 0.607°$, with FDFD as the only reference (2.28 and 3.56 million unknowns at 16 and 20 px/a, censuses certified on the FDFD matrix). The a-priori census says 51 in-domain states; FDFD finds 51 below the ceiling, all M_2-dominant. The exact-frame single-band model, one exact Bloch function of the registry-averaged monolayer per in-domain folded momentum, matches all 51 one to one with deviations between 4.7×10^{-8} and 8.1×10^{-8} in frequency, median 5.8×10^{-8}, while the measured error of the reference itself is between 3.2×10^{-8} and 5.2×10^{-8}. The comparison is reference-limited: the envelope model matches the full-Maxwell solver to within the solver's own discretization error on every state it claims, with the counts fixed before the comparison. The fixed-frame model lands its 13 a-priori rungs inside its declared 10^{-5} limit, but its count below the ceiling (59) does not close against the census (51).

Is the exact frame an addition to the theory or already inside it? It is inside it. The η^2 Löwdin dressing of Eq. (16) is the second-order piece of the resummed frame, and the remote-band content it carries is exactly the heavy mass the fixed frame lacks: the raw fixed-frame surface is an isotropic parabola of curvature 0.247, equal to the true light-direction curvature 0.2464, while

the heavy curvature 2.350 is carried entirely by the second-order $\boldsymbol{k} \cdot \boldsymbol{p}$ sum, which closes to 10^{-5}. Figure 14 in the appendix measures the ladder of orders on the 21 in-domain rungs at $(32, 31)$: medians in frequency of 8.3×10^{-4} for the raw fixed frame, 3.8×10^{-5} with the η^2 fold over one remote band, 9.9×10^{-6} with three, 2.1×10^{-6} with the exact Feshbach downfold of the same content, and 4.4×10^{-10} with resummed frames. The term the theory already contains recovers two to three decades, monotonically on every heavy rung; the remote content must be folded into the retained block and never jointly diagonalized.

The resummed-frame model Eq. (21), implemented as a standalone monolayer computation with no supercell anywhere, reproduces the supercell-built exact-frame model to 10^{-14} in λ and the 51-rung result of Fig. 3 in under a second on a laptop core. Its remaining error, the registry dressing of the frames, follows a clean a_2^2 law over a sweep of the interlayer amplitude at fixed angle, full window, all valleys: a median of 7.6×10^{-9} at $a_2 = 0.008$, 1.8×10^{-6} at 0.12 and 5.3×10^{-6} at 0.20 (Fig. 15 in the appendix). At the candidate material the valley-agnostic model matches all 51 states of the gap window at or below 8.6×10^{-6}, and with a trial buffer above the claim edge the maximum in-domain deviation at $(32, 31)$ is 1.8×10^{-9}, so the 5.8×10^{-8} median of Fig. 3 is the reference's floor, not the model's.

7 Dirac Geometry and the Search for Magic Angles

The K-point Dirac cone of a honeycomb crystal is the standard platform of photonic moiré physics [6, 8, 10] and the setting the multi-band expansion was built for. The crystal is a honeycomb of air rods of radius $0.408a$ in $\epsilon = 3.78$, TM polarization; its two sublattices play the roles of the two layers. The carrier is the zone corner $K = (2/3, 1/3)$ in fractional reciprocal coordinates, where the Dirac pair is bands 1 and 2 (zero-based) at $f_D = 0.6394$; the point $(1/3, 1/3)$, which fractional coordinates invite as a guess for K, is an interior point where bands 2 and 3 are accidentally near-degenerate, and a pair extracted there is not the Dirac pair. The Berry connection is the registry derivative of the retained frame, and eigensolver frames at neighbouring registries carry arbitrary phases and, inside a near-degenerate pair, arbitrary mixings whose finite differences are noise. The pair frame is therefore transported along the registry grid by removing the unitary polar factor of the overlap with the previous frame, and every retained block of the Hamiltonian is rotated into that gauge before assembly; the gauge-invariant quantities, inter-band gap, velocity norm, Born–Huang potential, quantum-metric trace and plaquette Berry curvature, serve as the check (Figs. 18 and 19 in the appendix). The Dirac gap closes at the aligned registry and opens to 0.14 where the sublattices are maximally displaced; Born–Huang potential and quantum metric peak at the degeneracy and along the three lines through it; the transported Berry connection is two orders of magnitude smaller than the raw one away from the degeneracy; and the plaquette curvature is antisymmetric across the degeneracy, as a two-band touching demands. The 48×48 registry grid is converged to about 10^{-4} in frequency, the level of the miniband widths of this crystal (Figs. 16 and 17).

Figure 4 scans the miniband bandwidth over 237 angles between $0.2°$ and $10°$; at each angle the envelope problem of the pair is solved at nine $\boldsymbol{q}$-points along Γ–M–K–Γ of the moiré zone for the twenty eigenvalues nearest the Dirac energy, with eight remote bands in the Löwdin mass tensor. Above $1.5°$ the RMS bandwidth follows $\theta^{1.6}$, between the linear law of a velocity-dominated envelope and the quadratic law of a mass-dominated one, as the coexistence of both terms in Eq. (18) predicts. Below $1.5°$ it settles on a plateau between 5×10^{-5} and 2×10^{-4} with a shallowest value of 5×10^{-5} at $1.05°$, a factor of three below the plateau's upper edge and not a collapse; the plateau is a resolution effect, since at a fixed number of grid points the twenty modes sample an ever denser ladder of minibands whose widths fall below the level spacing. No magic angle is found, and the reason is structural: in the Bistritzer–MacDonald model the magic angle occurs where the interlayer coupling matches the Dirac velocity, whereas here the coupling

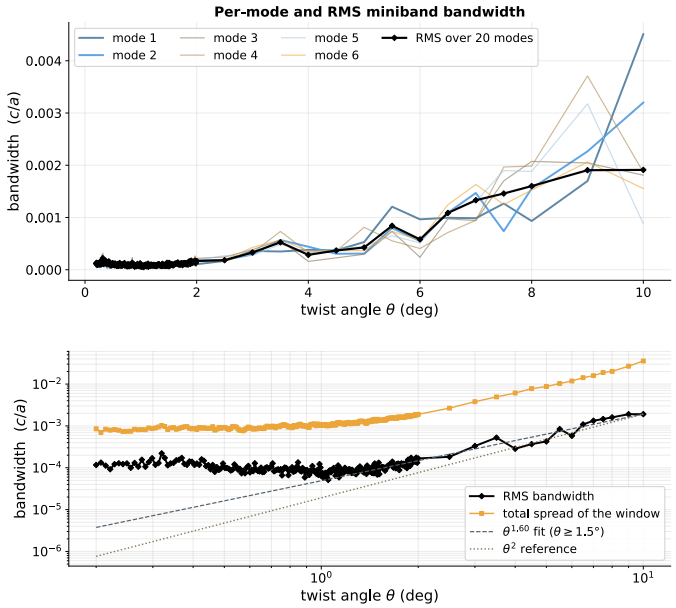

Figure 4: Moiré miniband bandwidth against the twist angle for the honeycomb TM Dirac pair at K (237 angles, nine $\boldsymbol{q}$-points, twenty modes around the Dirac energy). *Top*: per-mode bandwidth of the six lowest modes and the RMS over all twenty. *Bottom*: RMS bandwidth and total spread of the window on logarithmic axes, with the power law fitted above 1.5° and a θ^2 reference.

the twist modulates is the registry dependence of the local band data, which is weak against the Dirac velocity at every angle inside the validity window of Eq. (6). Whether a bilayer of two honeycomb crystals with a genuine interlayer coupling has a photonic magic angle within reach of the framework is left open.

8 Conclusion

The two-scale envelope approximation developed here replaces the global problem by a family of periodic two-atomic crystals connected by the registry map $\boldsymbol{\delta} = -J\boldsymbol{R}$ and projects the Maxwell operator onto their local Bloch modes. The effective Hamiltonian Eq. (18), for TE and TM, carries band energies, velocities, a Löwdin-dressed mass tensor, a non-Abelian Berry connection and an ϵ^{-1}-weighted Born–Huang potential, all defined on the registry torus and independent of the twist angle; its all-orders limit is the resummed-frame model Eq. (21), a monolayer computation with no supercell anywhere.

On an isolated manifold with weak interlayer coupling the envelope model is exact to the precision of the best full-Maxwell solvers, with measured error laws in the angle and in the coupling; on the strongly coupled square bilayer it reproduces the manifold floor within MPB's own error and is the only solver below 2°; and the registry-domain geometry of a honeycomb Dirac crystal, in a consistent gauge, decomposes the moiré physics in a way no supercell solver offers, with no magic angle inside the window where the theory applies.

Three items remain open: a point-group-covariant gauge for the registry-adapted frames, so that the tower of the strongly coupled crystal is reproduced with its degeneracies; the next order of the theory, registry-dependent frames at every harmonic, which is defined and was not needed in the materials studied here; and the extension of the two-scale formalism to slab geometries with evanescent interlayer coupling, where most experimental moiré photonics operates. The pipeline, the solver and the data are open source [29, 32, 33].

A The Effective Hamiltonians in Full

Full TE Effective Hamiltonian

η^0 zeroth order η^1 first order η^2 second order band energies group velocity Berry connection inverse mass tensor Born-Huang potential Löwdin remote-band pieces

$$\mathcal{H}_{\text{eff}} = \Big[\underbrace{\Lambda}_{\text{band energies}}\Big] + \eta\Big[\underbrace{\tfrac{1}{2}\big(v^{(i)}\,\Pi_i + \Pi_i\,v^{(i)}\big)}_{\text{group velocity}\,\cdot\,\text{covariant momentum}} + \underbrace{\Xi^{(1)}_{\text{sc}} + \tfrac{\mathrm{i}}{2}\,\partial_{R_i}v^{(i)} + \tfrac{1}{2}\,[A_i, v^{(i)}]}_{\text{first-order remainder}\ +U^{(1)}_{\text{rem}}}\Big]$$

$$+\eta^2\Big[\underbrace{\tfrac{1}{2}\,\Pi_i\,M^{-1}_{ij}\,\Pi_j}_{\text{inverse mass tensor}\ +\ (\text{Löwdin downfolded})} + \underbrace{\Xi_i^\dagger\,\varepsilon^{-1}\,\Xi_i}_{\text{Born-Huang}} + \underbrace{K_i^\dagger\,\mathcal{D}_i - \mathcal{D}_i\,K_i}_{\text{direct 1-deriv. remainder}} + \underbrace{\mathcal{D}_i\,\mathcal{T}_i^\dagger\,R_Q\,\mathcal{R} - \mathcal{R}^\dagger\,R_Q\,\mathcal{T}_i\,\mathcal{D}_i}_{\text{Löwdin 1-deriv. cross}} - \underbrace{\mathcal{R}^\dagger\,R_Q\,\mathcal{R}}_{\text{Löwdin scalar}}\Big] + O(\eta^3)$$

slow derivatives act on everything to their right, coefficient fields included; the second-order bracket is the flux form of the direct term plus $-S^\dagger R_Q S$ for the remote-band excursion (equivalent to the raw split with $\Gamma^{(2)}$, not additional to it)

where

gauge-covariant slow momentum, slow covariant derivative, and Berry connection (in P-space)

$$\Pi_i = -\mathrm{i}\,\mathcal{D}_i\,, \quad \mathcal{D}_i = D_{R_i} - \mathrm{i}\,A_i\,, \quad A_i = \mathrm{i}\,U^\dagger\,\partial_{R_i}U$$

Löwdin-corrected inverse mass tensor; bare metric $G_{mn} = \langle u_m, \varepsilon^{-1}u_n\rangle_\Omega$

$$\big(M^{-1}_{ij}\big)_{mn} = 2\,\delta_{ij}\,G_{mn} + \sum_{\ell\notin P}\left[\frac{v^{(i)}_{m\ell}v^{(j)}_{\ell n}}{\lambda_n - \lambda_\ell} + \frac{v^{(j)}_{m\ell}v^{(i)}_{\ell n}}{\lambda_m - \lambda_\ell}\right]$$

direct one-derivative coefficient (flux form of $-D_{R_i}\varepsilon^{-1}D_{R_i}$ projected on U)

$$K_i = U^\dagger\,\varepsilon^{-1}\,\Xi_i\,, \quad \mathcal{H}^{(2)}_{\text{dir}} = -\mathcal{D}_i(G\mathcal{D}_i + K_i) + K_i^\dagger\mathcal{D}_i + \Xi_i^\dagger\varepsilon^{-1}\Xi_i$$

remote-band excursion (manifestly Hermitian; expanded into the three Löwdin pieces above)

$$S = \mathcal{T}_i\,\mathcal{D}_i + \mathcal{R}\,, \quad \mathcal{H}^{(2)}_{\text{remote}} = -S^\dagger\,R_Q\,S$$

velocity matrix elements and TE velocity operator (action on a test field φ)

$$v^{(i)}_{mn} = \langle u_m, \mathcal{V}_i\,u_n\rangle_\Omega\,, \quad \mathcal{V}_i\,\varphi = -\mathrm{i}\left[D_{r_i}(\varepsilon^{-1}\varphi) + \varepsilon^{-1}D_{r_i}\varphi\right]$$

out-of-subspace frame leakage and first-order scalar remainder

$$\Xi_i = Q\,\partial_{R_i}U\,, \quad \Xi^{(1)}_{\text{sc}} = -\sum_i\left[\mathrm{i}\,U^\dagger\,\mathcal{V}_i\,\Xi_i + U^\dagger\left(\partial_{R_i}\varepsilon^{-1}\right)D_{r_i}\,U\right]$$

Löwdin coupling operators (P–Q channels) and reduced resolvent

$$\mathcal{T}_i = -\mathrm{i}\,Q\,\mathcal{V}_i\,U\,, \quad R_Q = \left[Q\left(\mathcal{L}^{(0)}_{\text{TE}} - \lambda_{\text{ref}}\right)Q\right]^{-1}, \quad \mathcal{R} = -Q\left[\mathrm{i}\,\mathcal{V}_i\,\Xi_i + \left(\partial_{R_i}\varepsilon^{-1}\right)D_{r_i}\,U\right]$$

Born-Huang leakage potential (ε^{-1}-weighted form is exact)

$$U_{\text{BH,exact}} = \Xi_i^\dagger\,\varepsilon^{-1}\,\Xi_i\,, \quad U_{\text{BH}} \approx \Xi_i^\dagger\,\Xi_i \quad \text{(unweighted approximation)}$$

$P = U\,U^\dagger$ (retained-band projector) | $Q = 1 - P$ (remote complement) | $U(\boldsymbol{R})$: retained Bloch frame, columns u_n | $D_{r_i} = \partial_{r_i} + \mathrm{i}\,k_{0,i}$ (fast cov. deriv.) | $D_{R_i} = \partial_{R_i} + \mathrm{i}\,q_i$ (slow cov. deriv.) | φ: smooth test field | $\langle\cdot,\cdot\rangle_\Omega$: fast-cell inner product

Figure 5: The complete TE effective Hamiltonian Eq. (18) with every term written out. Bracket colours mark the order in η; term colours mark the named ingredients and the Löwdin remote-band pieces. The second-order bracket is the flux form Eq. (17) plus the remote-band excursion $-S^\dagger R_Q S$ of Eq. (26); slow derivatives act on everything to their right.

Full TM Effective Hamiltonian

η^0 zeroth order η^1 first order η^2 second order band energies hermitized velocity Berry connection inverse mass tensor Born-Huang potential Löwdin remote-band pieces hermitizing factor ρ

$$\mathcal{H}_{\mathrm{TM,eff}} = \Big[\underbrace{\Lambda}_{\text{band energies}}\Big] + \eta\Big[\underbrace{\tfrac{1}{2}\big(\tilde{v}^{(i)}\,\Pi_i + \Pi_i\,\tilde{v}^{(i)}\big)}_{\text{hermitized velocity}\,\cdot\,\text{covariant momentum}} + \underbrace{\tilde{\Xi}^{(1)}_{\mathrm{sc}} + \tfrac{\mathrm{i}}{2}\,\partial_{R_i}\tilde{v}^{(i)} + \tfrac{1}{2}\,[A_i,\tilde{v}^{(i)}]}_{\text{first-order remainder}\ +U^{(1)}_{\mathrm{rem}}}\Big]$$

$$+\eta^2\Big[\underbrace{\tfrac{1}{2}\,\Pi_i\,\widetilde{M}^{-1}_{ij}\,\Pi_j}_{\text{inverse mass tensor}\ +\ (\text{Löwdin downfolded})} + \underbrace{Y_i^\dagger\,Y_i}_{\text{Born-Huang (TM)}} + \underbrace{\tilde{K}_i^\dagger\,\mathcal{D}_i - \mathcal{D}_i\,\tilde{K}_i}_{\text{direct 1-deriv. remainder}} + \underbrace{\mathcal{D}_i\,\tilde{\mathcal{T}}_i^\dagger\,R_Q\,\tilde{\mathcal{R}} - \tilde{\mathcal{R}}^\dagger\,R_Q\,\tilde{\mathcal{T}}_i\,\mathcal{D}_i}_{\text{Löwdin 1-deriv. cross}} - \underbrace{\tilde{\mathcal{R}}^\dagger\,R_Q\,\tilde{\mathcal{R}}}_{\text{Löwdin scalar}}\Big] + O(\eta^3)$$

acts on the hermitized envelope $\tilde{\boldsymbol{f}}$ of $\tilde{\psi} = \varepsilon^{1/2}\psi$; slow derivatives act on everything to their right; same flux-form and $-\tilde{S}^\dagger R_Q \tilde{S}$ bookkeeping as the TE poster, every coefficient dressed by ρ

where

gauge-covariant slow momentum, slow covariant derivative, and Berry connection of the hermitized frame

$$\Pi_i = -\mathrm{i}\,\mathcal{D}_i\,, \quad \mathcal{D}_i = D_{R_i} - \mathrm{i}\,A_i\,, \quad A_i = \mathrm{i}\,\tilde{U}^\dagger\,\partial_{R_i}\tilde{U}$$

Löwdin-corrected inverse mass tensor; weighted metric $\tilde{G}_{mn} = \langle \tilde{u}_m, \varepsilon^{-1}\tilde{u}_n\rangle_\Omega$

$$\big(\widetilde{M}^{-1}_{ij}\big)_{mn} = 2\,\delta_{ij}\,\tilde{G}_{mn} + \sum_{\ell\notin P}\left[\frac{\tilde{v}^{(i)}_{m\ell}\tilde{v}^{(j)}_{\ell n}}{\lambda_n - \lambda_\ell} + \frac{\tilde{v}^{(j)}_{m\ell}\tilde{v}^{(i)}_{\ell n}}{\lambda_m - \lambda_\ell}\right]$$

direct one-derivative coefficient (flux form of $-\rho D_{R_i} D_{R_i}\rho$ projected on $\tilde{U}$)

$$\tilde{K}_i = \tilde{U}^\dagger\,\rho\,Y_i\,, \quad \tilde{\mathcal{H}}^{(2)}_{\mathrm{dir}} = -\mathcal{D}_i\big(\tilde{G}\mathcal{D}_i + \tilde{K}_i\big) + \tilde{K}_i^\dagger\mathcal{D}_i + Y_i^\dagger Y_i$$

remote-band excursion (manifestly Hermitian; expanded into the three Löwdin pieces above)

$$\tilde{S} = \tilde{\mathcal{T}}_i\,\mathcal{D}_i + \tilde{\mathcal{R}}\,, \quad \tilde{\mathcal{H}}^{(2)}_{\mathrm{remote}} = -\tilde{S}^\dagger\,R_Q\,\tilde{S}$$

hermitized velocity operator (action on a test field φ) and its matrix elements

$$\tilde{\mathcal{V}}_i\,\varphi = -2\mathrm{i}\,\rho\,D_{r_i}(\rho\,\varphi) = -2\mathrm{i}\,\varepsilon^{-1}D_{r_i}\varphi + \mathrm{i}\,\varepsilon^{-2}\big(\partial_{r_i}\varepsilon\big)\,\varphi\,, \quad \tilde{v}^{(i)}_{mn} = \langle \tilde{u}_m, \tilde{\mathcal{V}}_i\,\tilde{u}_n\rangle_\Omega$$

frame leakage, TM leakage flux (carries the slow variation of ρ; no TE analogue), first-order scalar remainder

$$\tilde{\Xi}_i = Q\,\partial_{R_i}\tilde{U}\,, \quad Y_i = \rho\,\tilde{\Xi}_i + \big(\partial_{R_i}\rho\big)\,\tilde{U}\,, \quad \tilde{\Xi}^{(1)}_{\mathrm{sc}} = -\sum_i\Big[\mathrm{i}\,\tilde{U}^\dagger\,\tilde{\mathcal{V}}_i\,\tilde{\Xi}_i + 2\,\tilde{U}^\dagger\,\rho\,D_{r_i}\big(\big(\partial_{R_i}\rho\big)\,\tilde{U}\big)\Big]$$

Löwdin coupling operators (P–Q channels) and reduced resolvent of the hermitized local operator

$$\tilde{\mathcal{T}}_i = -\mathrm{i}\,Q\,\tilde{\mathcal{V}}_i\,\tilde{U}\,, \quad R_Q = \Big[Q\,\big(\tilde{\mathcal{H}}^{(0)}_{\mathrm{TM}} - \lambda_{\mathrm{ref}}\big)\,Q\Big]^{-1}\,, \quad \tilde{\mathcal{R}} = -Q\,\Big[\mathrm{i}\,\tilde{\mathcal{V}}_i\,\tilde{\Xi}_i + 2\,\rho\,D_{r_i}\big(\big(\partial_{R_i}\rho\big)\,\tilde{U}\big)\Big]$$

TM Born-Huang potential, expanded (ε^{-1}-weighted leakage plus the hermitizing-factor terms)

$$U_{\mathrm{BH,TM}} = Y_i^\dagger Y_i = \tilde{\Xi}_i^\dagger\,\varepsilon^{-1}\,\tilde{\Xi}_i + \big[\tilde{\Xi}_i^\dagger\,\rho\,\big(\partial_{R_i}\rho\big)\,\tilde{U} + \mathrm{h.c.}\big] + \tilde{U}^\dagger\,\big(\partial_{R_i}\rho\big)^2\,\tilde{U}$$

$\rho = \varepsilon^{-1/2}$, $\tilde{u}_n = \varepsilon^{1/2}u_n^{\mathrm{TM}}$ (hermitized local Bloch states, plain-orthonormal) | $\tilde{\mathcal{H}}^{(0)}_{\mathrm{TM}} = -\rho\,D_{\boldsymbol{r}}\cdot D_{\boldsymbol{r}}\,\rho$ | $P = \tilde{U}\,\tilde{U}^\dagger$, $Q = 1 - P$ | $D_{r_i} = \partial_{r_i} + \mathrm{i}\,k_{0,i}$, $D_{R_i} = \partial_{R_i} + \mathrm{i}\,q_i$ | $\langle\cdot,\cdot\rangle_\Omega$: fast-cell inner product

Figure 6: The complete TM effective Hamiltonian in the same layout. Every coefficient carries the hermitizing factor $\rho = \epsilon^{-1/2}$, and the leakage flux Y_i of Eq. (20) collects the slow variation of ρ that has no TE analogue. The coefficient identities are listed in Appendix B.

B Downfolding and Coefficient Identities

Slow derivatives act on everything to their right, including the $\boldsymbol{R}$-dependence of coefficient operators, and $\mathcal{D}_i^\dagger = -\mathcal{D}_i$ on the moiré torus. The exact first-order projected operator is $-\mathrm{i}\, v^{(i)}\mathcal{D}_i + \Xi_{\mathrm{sc}}^{(1)}$ with

$$\Xi_{\mathrm{sc}}^{(1)} := -\sum_{i=x,y}\Big[\mathrm{i}\, U^\dagger \mathcal{V}_i \Xi_i + U^\dagger\big(\partial_{R_i}\epsilon^{-1}\big) D_{r_i} U\Big], \tag{24}$$

and rewriting it as the symmetrized drift of Eq. (15) leaves the remainder $U_{\mathrm{rem}}^{(1)}$ stated there. For the remote-band term define

$$\mathcal{T}_i := -\mathrm{i}\, Q\mathcal{V}_i U, \qquad \mathcal{R} := -Q\Big[\mathrm{i}\,\mathcal{V}_i\Xi_i + \big(\partial_{R_i}\epsilon^{-1}\big) D_{r_i} U\Big], \qquad S := \mathcal{T}_i\mathcal{D}_i + \mathcal{R} = Q\mathcal{L}^{(1)}U, \tag{25}$$

so that the excursion in Eq. (14) is manifestly Hermitian,

$$-U^\dagger\mathcal{L}^{(1)}Q\, R_Q\, Q\mathcal{L}^{(1)}U = -S^\dagger R_Q S = \mathcal{D}_i\big(\mathcal{T}_i^\dagger R_Q \mathcal{T}_j\, \mathcal{D}_j + \mathcal{T}_i^\dagger R_Q\mathcal{R}\big) - \mathcal{R}^\dagger R_Q \mathcal{T}_i\, \mathcal{D}_i - \mathcal{R}^\dagger R_Q \mathcal{R}. \tag{26}$$

The first term is the remote-band kinetic correction, $-\Pi_i\, \mathcal{T}_i^\dagger R_Q \mathcal{T}_j\, \Pi_j$ with $(\mathcal{T}_i^\dagger R_Q \mathcal{T}_j)_{mn} = \sum_{\ell\notin P} v_{m\ell}^{(i)} v_{\ell n}^{(j)}/(\lambda_\ell - \lambda_{\mathrm{ref}})$, which reproduces the Löwdin sum of Eq. (16) once λ_{ref} is replaced by the retained band energies; the second and third terms are one-derivative cross remainders, the last is the scalar remainder. Because the coefficient operators depend on $\boldsymbol{R}$, a split with the derivatives pulled in front of frozen coefficients is neither an operator identity nor Hermitian. The direct second-order operator admits two complete bookkeepings: the raw split $-G\, D_{R_i}^2 - B^{(i)} D_{R_i} + \Gamma^{(2)}$ with $G_{mn} = \langle u_m,\, \epsilon^{-1}u_n\rangle_\Omega$, $B_{mn}^{(i)} = \langle u_m,\, \partial_{R_i}(\epsilon^{-1}u_n) + \epsilon^{-1}\partial_{R_i}u_n\rangle_\Omega$ and $\Gamma_{mn}^{(2)} = -\sum_i \langle u_m,\, \partial_{R_i}(\epsilon^{-1}\partial_{R_i}u_n)\rangle_\Omega$, and the flux form Eq. (17). The two are equal; the scalar $\Gamma^{(2)}$ is contained in the leakage and K terms of the flux form, and the two forms must never be added. For TM the same identities hold for the hermitized frame $\tilde U$, with $\tilde{\mathcal{V}}_i\phi = -2\mathrm{i}\,\rho D_{r_i}(\rho\phi) = -2\mathrm{i}\,\epsilon^{-1}D_{r_i}\phi + \mathrm{i}\,\epsilon^{-2}(\partial_{r_i}\epsilon)\phi$ and

$$\begin{aligned}\tilde\Xi_{\mathrm{sc}}^{(1)} &:= -\sum_{i=x,y}\Big[\mathrm{i}\,\tilde U^\dagger\tilde{\mathcal{V}}_i\tilde\Xi_i + 2\,\tilde U^\dagger\rho D_{r_i}\big((\partial_{R_i}\rho)\tilde U\big)\Big],\\ \tilde{\mathcal{T}}_i &:= -\mathrm{i}\, Q\tilde{\mathcal{V}}_i\tilde U, \qquad \tilde{\mathcal{R}} := -Q\Big[\mathrm{i}\,\tilde{\mathcal{V}}_i\tilde\Xi_i + 2\rho D_{r_i}\big((\partial_{R_i}\rho)\tilde U\big)\Big],\end{aligned} \tag{27}$$

$\tilde S := \tilde{\mathcal{T}}_i\mathcal{D}_i + \tilde{\mathcal{R}}$ and the reduced resolvent of the hermitized local operator. The direct part takes the flux form $-\mathcal{D}_i(\tilde G\,\mathcal{D}_i + \tilde K_i) + \tilde K_i^\dagger\mathcal{D}_i + Y_i^\dagger Y_i$ with $\tilde K_i := \tilde U^\dagger\rho\, Y_i$, and the mass tensor is Eq. (16) with $\tilde v$ and $\tilde G$ in place of v and G. The terms proportional to $\partial_{R_i}\rho$ have no TE analogue.

C Supplementary Figures

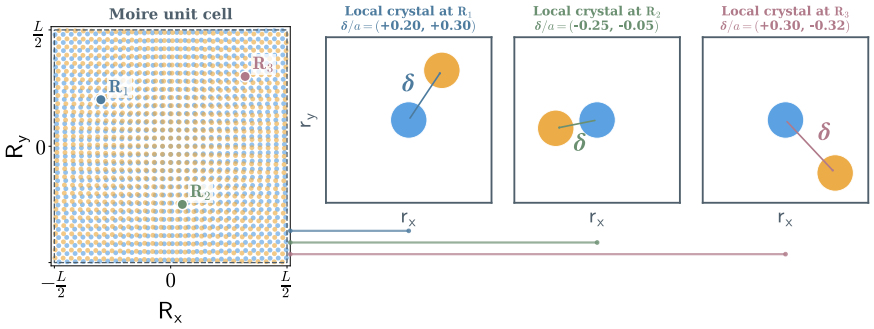

Figure 7: Any position $\boldsymbol{R}$ inside the moiré cell determines a local two-atomic crystal via the registry map $\boldsymbol{\delta}(\boldsymbol{R})$. The coloured arrows show $\boldsymbol{\delta}$ for three sample positions; the shift varies smoothly with $\boldsymbol{R}$, and each local cell spans $r_x, r_y \in [-a/2, a/2]$.

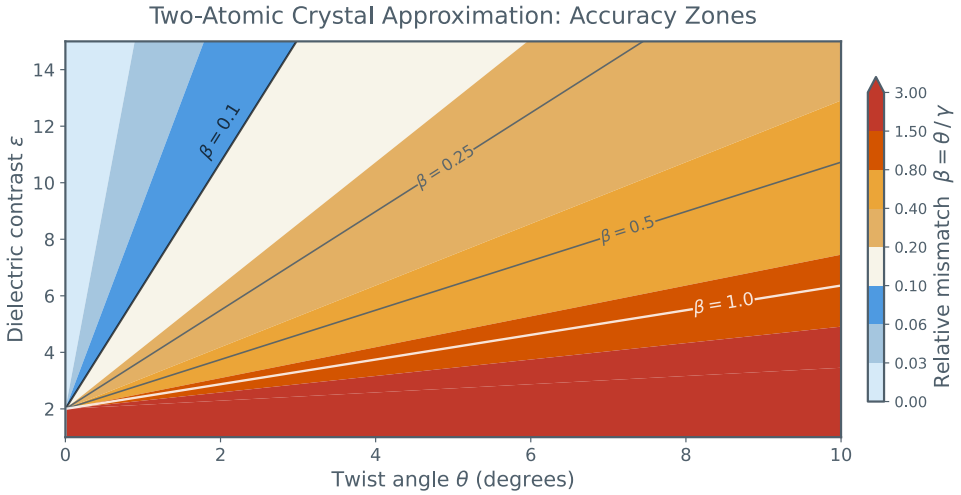

Figure 8: Accuracy zones of the two-atomic crystal approximation. Colour encodes the quality parameter $\beta = \theta/\gamma$ of Eq. (6), the accumulated registry mismatch at the Bragg penetration depth, over the twist angle and the dielectric contrast of TE square-lattice rods in air. The zone boundaries are conventional; the β contours are the quantitative criterion.

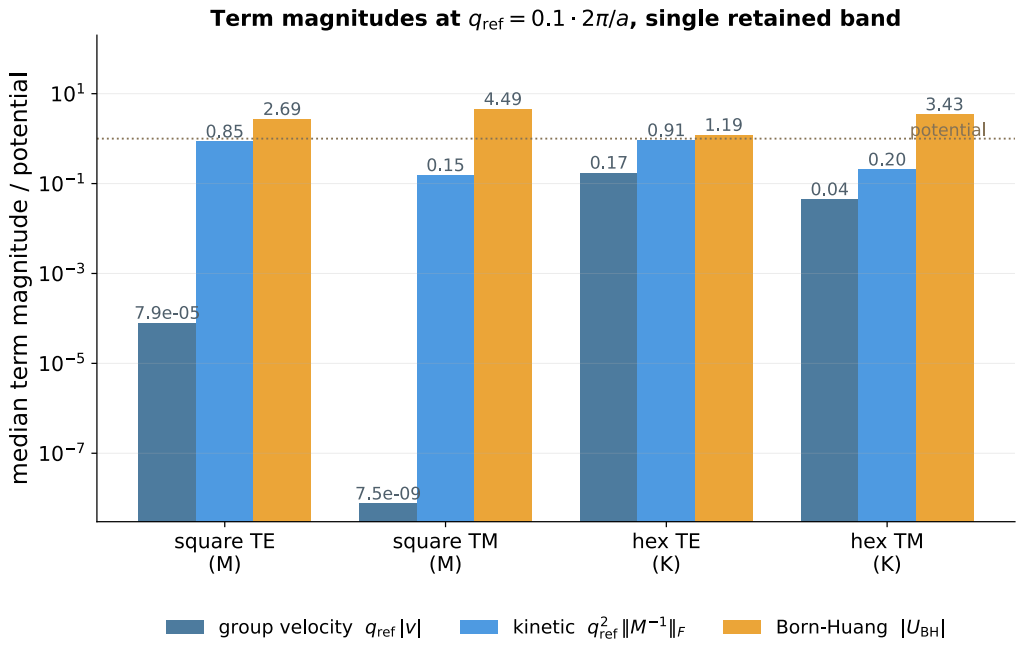

Figure 9: Median magnitudes over the registry grid of the effective-Hamiltonian terms at a characteristic moiré momentum $q_{\mathrm{ref}} = 0.1 \times 2\pi/a$, normalized to the local potential λ, for a single retained band. Square rods at M (TE, TM) and hexagonal holes at $K = (2/3, 1/3)$ (TE, TM). At M the velocity term vanishes by time-reversal symmetry; at K a single band acquires a first-order slope at generic registries. The Born–Huang term outweighs the kinetic term in every configuration.

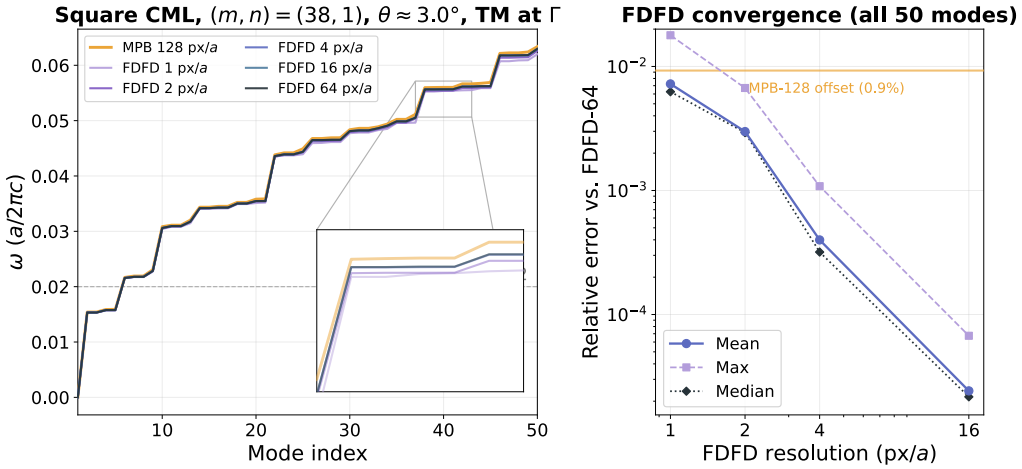

Figure 10: FDFD resolution convergence for a square-lattice supercell ($(m, n) = (38, 1)$, $\theta \approx 3.0°$, 1445 cells, TM at Γ, 50 lowest modes). *Left*: sorted eigenfrequencies against mode index, the MPB reference at 128 px/a overlaid with FDFD at 1 to 64 px/a; the inset zooms into modes 37 to 43. *Right*: mean, median and maximum relative error against FDFD-64 on logarithmic axes; the horizontal line marks the resolution-independent cross-method offset of about 0.9% against MPB-128.

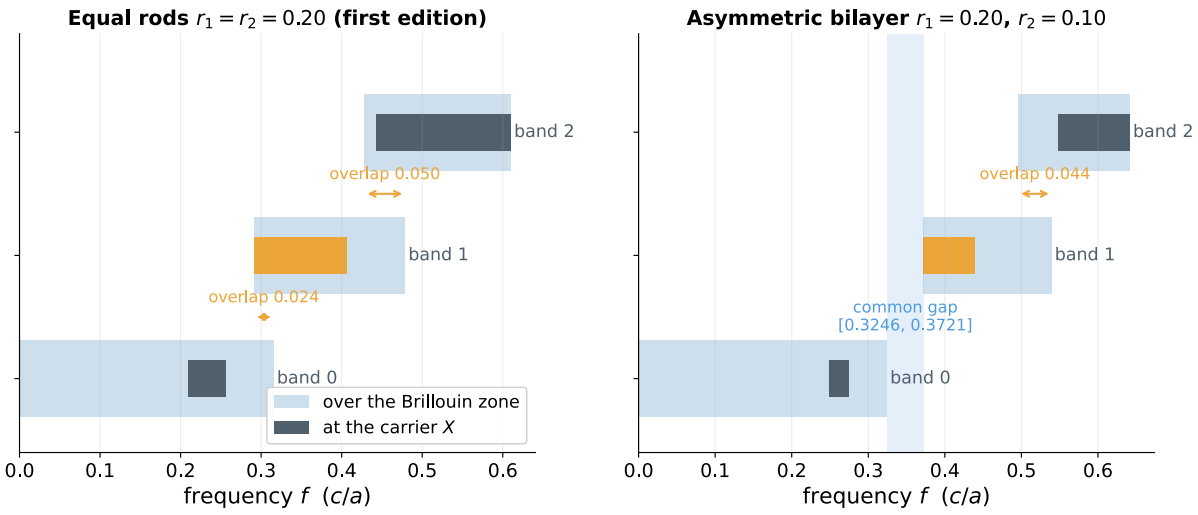

Figure 11: Registry-resolved band windows of the square TM bilayer at the carrier X and over the Brillouin zone, for the equal-rod crystal ($r_1 = r_2 = 0.20a$, left) and the asymmetric bilayer ($r_1 = 0.20a$, $r_2 = 0.10a$, right); $\epsilon = 8.9$ in both. Bars span the range of each band over a 5×5 registry grid; pale bars span the full zone. A registry-common gap exists only where the pale bar of band n ends below the pale bar of band $n+1$ begins. For equal rods the band-0 continuum overlaps the band-1 window at X and the manifold dissolves; the weak second layer restores the gap.

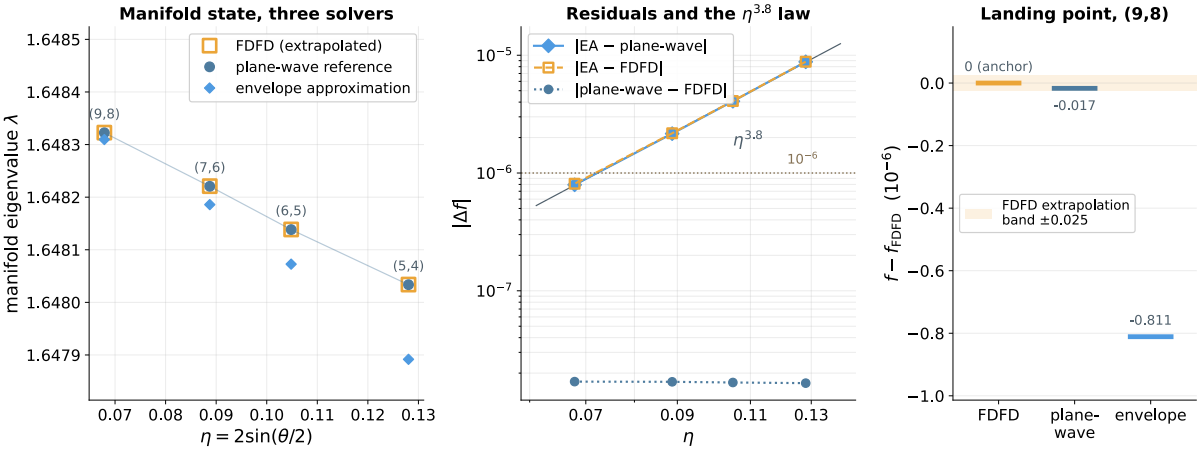

Figure 12: The manifold state across the scaled family of the smooth single-valley crystal. *Left*: its eigenvalue in FDFD (open squares), the plane-wave reference (dots) and the envelope model (diamonds). *Middle*: the residuals with the fitted power law and the 10^{-6} line. *Right*: the landing point at $(9, 8)$ on a 10^{-6} frequency axis, the FDFD extrapolation band shaded.

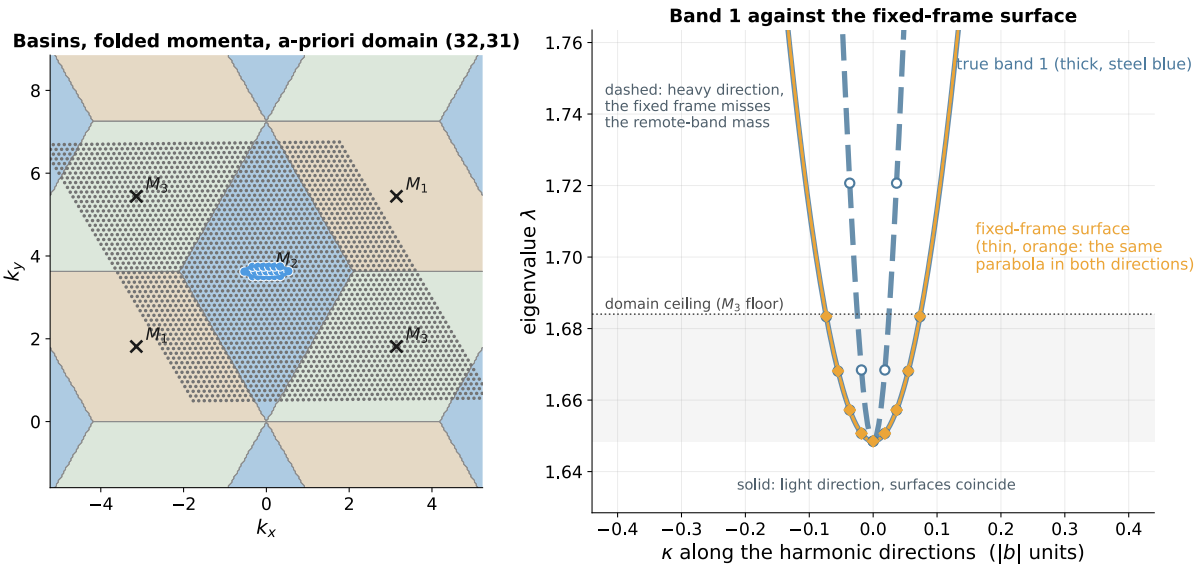

Figure 13: Momentum-space anatomy of the sector ladder at $(32, 31)$. *Left*: the monolayer zone around M_2 partitioned into the basins of the three M points, the folded momentum lattice of the commensuration (dots), and the a-priori domain of the single-valley envelope theory (filled circles): harmonics in the M_2 basin at or below the M_3 floor (contour). *Right*: the registry-averaged band 1 along the two principal harmonic directions (thick) against the fixed-frame envelope surface (thin). Along the light direction the two coincide and the rungs match at 10^{-7}; along the heavy direction the fixed frame misses the remote-band mass.

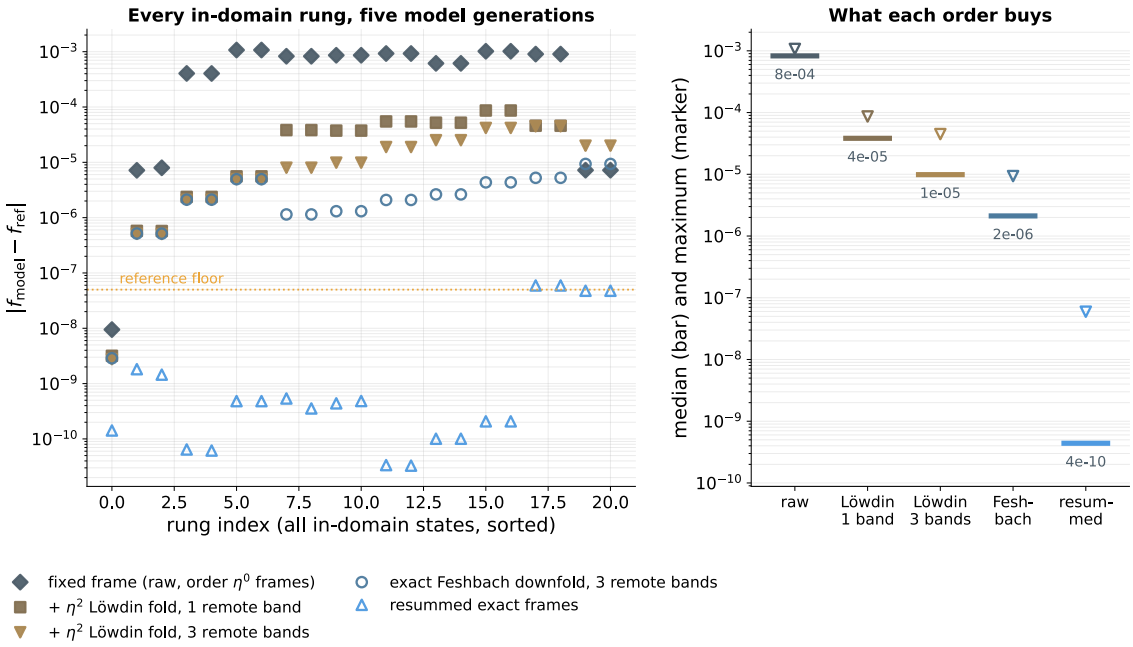

Figure 14: Completing the envelope approximation order by order at $(32, 31)$, scaled family, all 21 in-domain rungs. *Left*: per-rung deviation from the certified reference for the raw fixed frame, the fixed frame with the η^2 Löwdin fold over one and over three remote bands, the exact Feshbach downfold of the same three-band content, and the resummed exact frames. *Right*: medians (bars) and maxima (markers) of the same five models.

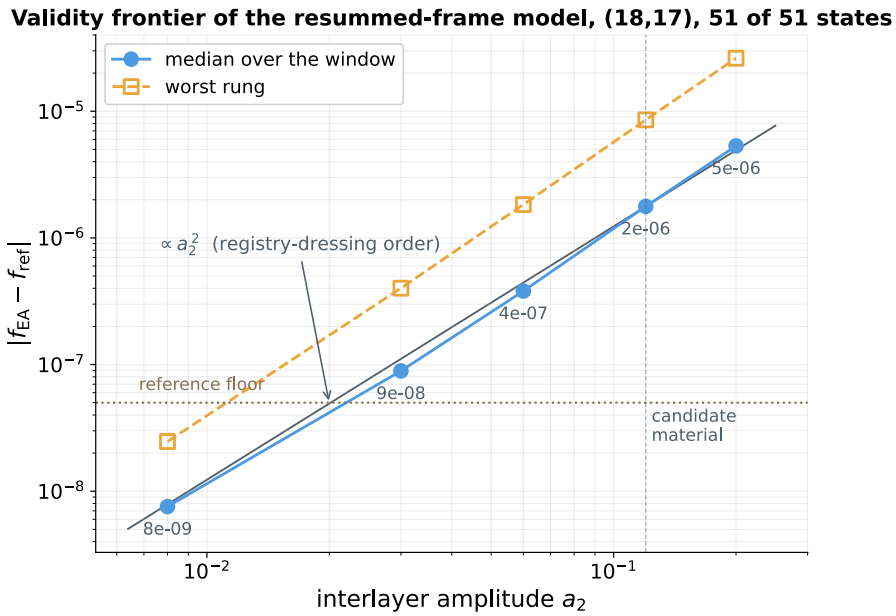

Figure 15: Validity frontier of the resummed-frame model at $(18, 17)$: median and worst deviation from the certified reference over the full gap window, all valleys, 51 of 51 states at every point, against the interlayer amplitude a_2. The grey line is the a_2^2 law of the registry-dressing order, pinned at the candidate material.

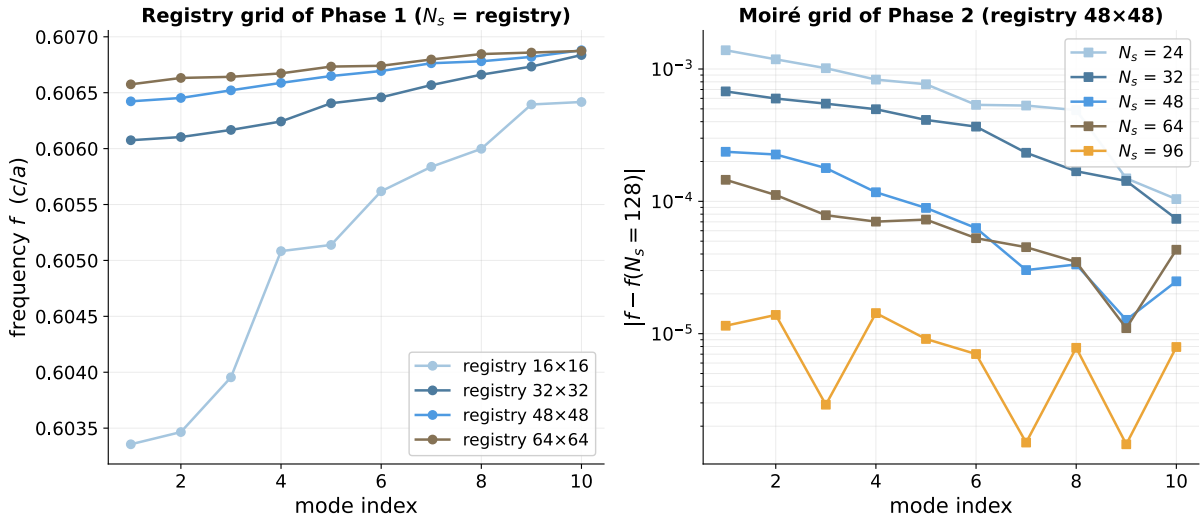

Figure 16: Convergence of the envelope eigenvalues of the honeycomb Dirac pair at $\theta = 1°$, moiré Γ point. *Left*: the ten lowest eigenvalues with the registry grid of Phase 1, the moiré grid locked to it. *Right*: deviation from the 128×128 moiré grid when only the Phase 2 grid is refined on fixed 48×48 registry data.

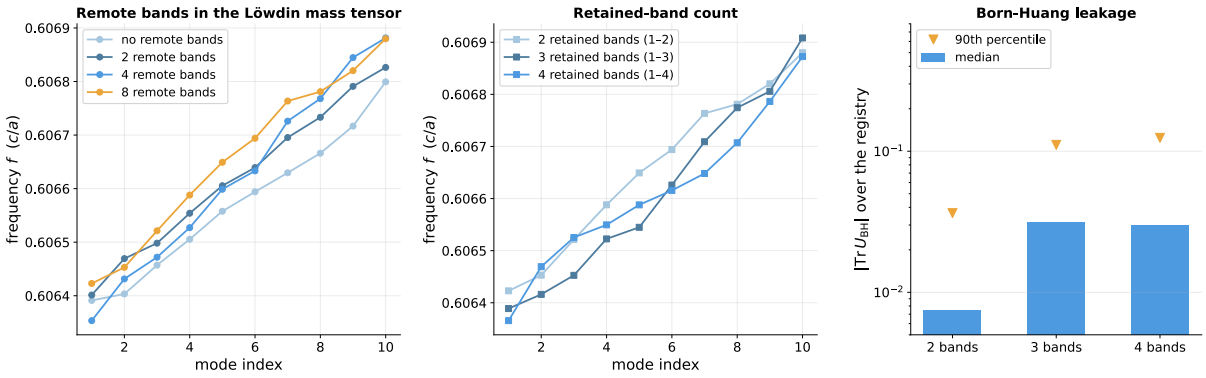

Figure 17: Sensitivity of the envelope spectrum of the honeycomb Dirac pair ($\theta = 1°$, Γ) to the band counts. *Left*: the ten lowest eigenvalues with zero, two, four and eight remote bands in the Löwdin mass tensor. *Middle*: the same with two, three and four retained bands. *Right*: median and 90th percentile of the Born–Huang trace over the registry for the three retained sets; the leakage reacts to a poorly isolated retained set long before the eigenvalues do.

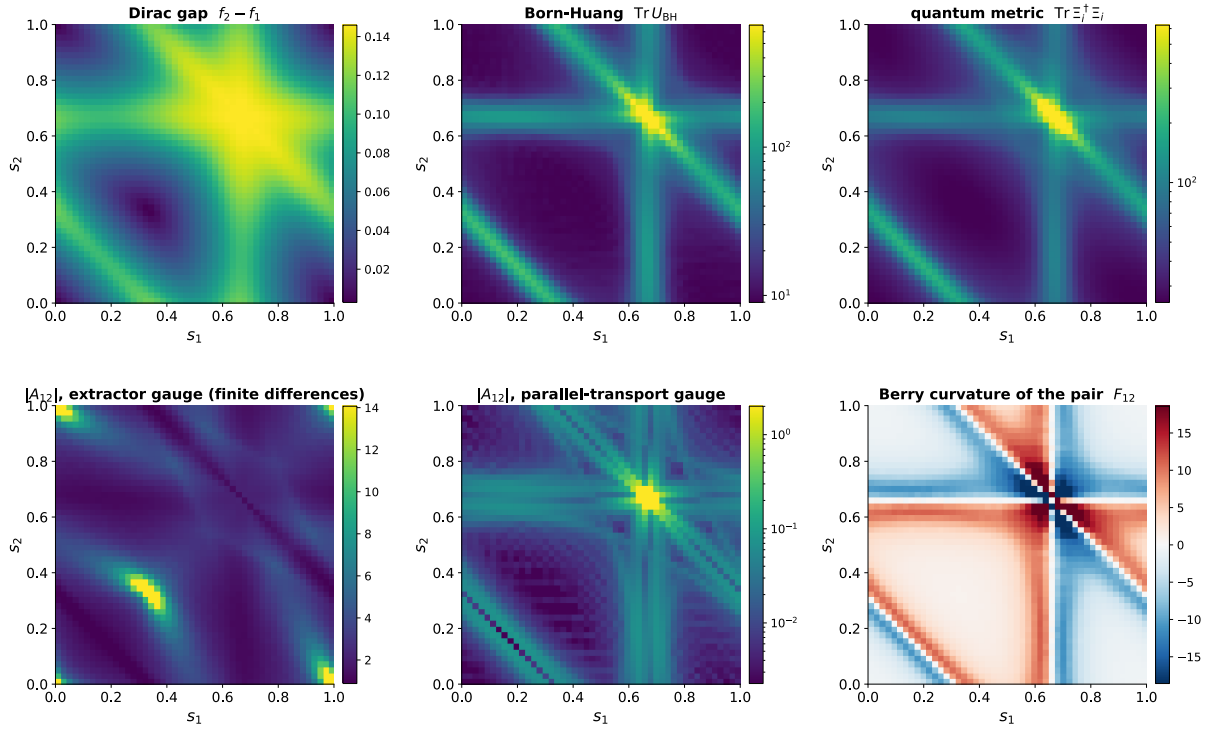

Figure 18: Registry-domain geometry of the Dirac pair of the honeycomb TM crystal at K (48×48 registry grid, resolution 64). *Top*: the gap between the two Dirac bands, the trace of the Born–Huang potential, and the trace of the quantum metric $\Xi_i^\dagger \Xi_i$ of the pair. *Bottom*: the Berry connection magnitude $|A_{12}|$ from finite differences in the eigensolver's own gauge, the same quantity in the parallel-transport gauge, and the gauge-invariant plaquette Berry curvature. The Dirac degeneracy sits at the aligned registry; the three lines of enhanced leakage through it are the registries where the two sublattices come closest.

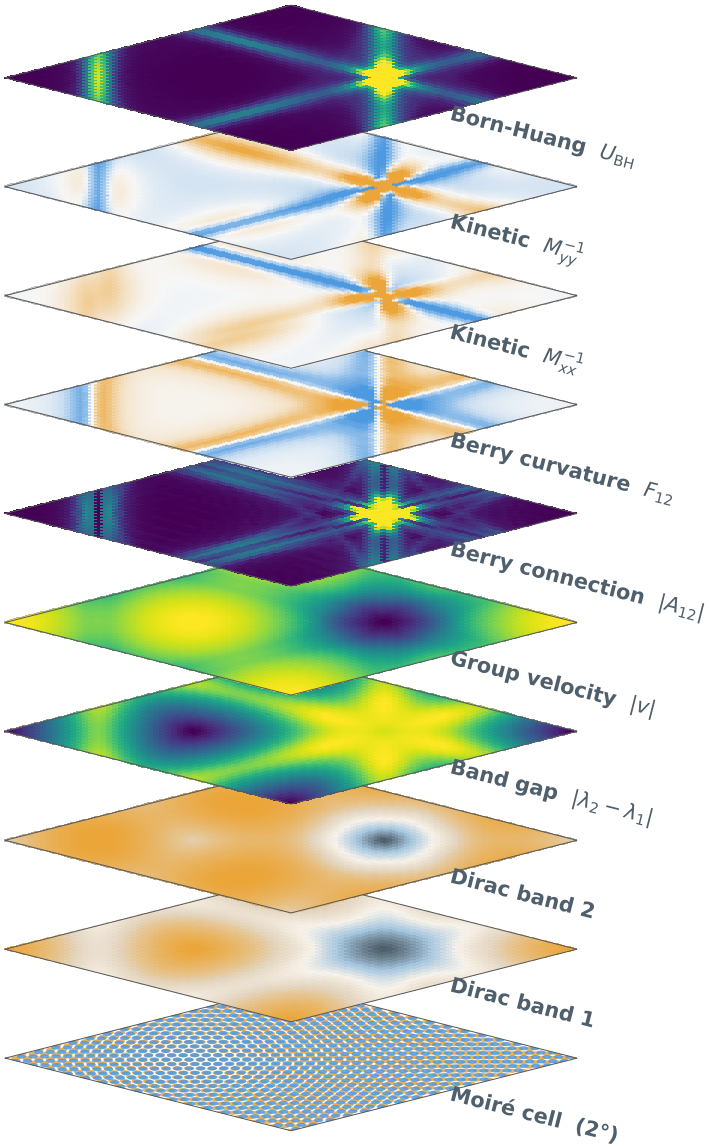

Figure 19: Full ingredient stack of the effective Hamiltonian for the honeycomb TM crystal at K: the moiré cell at 2°, the two Dirac bands over the registry torus, the inter-band gap, the velocity norm, the Berry connection $|A_{12}|$ in the parallel-transport gauge, the Berry curvature of the pair, both mass tensors with the Löwdin dressing by eight remote bands, and the Born–Huang potential. The 48×48 registry sweep resolves the full spatial structure across the moiré cell.

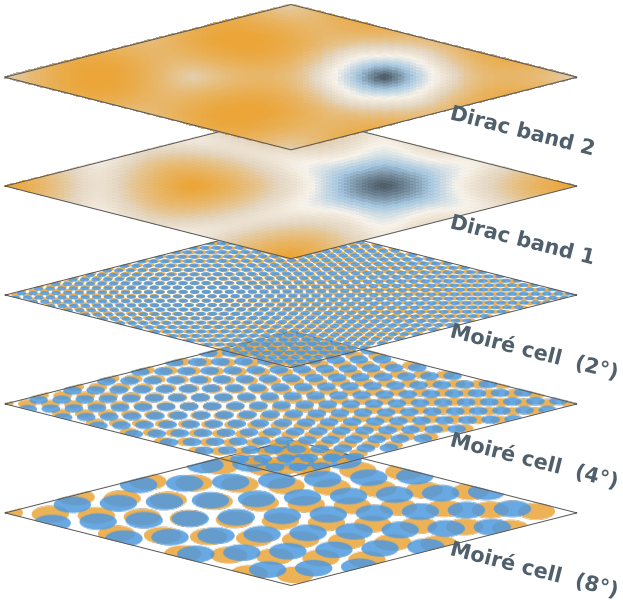

Figure 20: The two Dirac-band landscapes of the honeycomb TM crystal stacked above the moiré cells at 8°, 4° and 2°. The registry data are independent of the twist angle; only the cell they are mapped onto changes with θ, which is the Phase 1 invariance of Sec. 4 made visible.

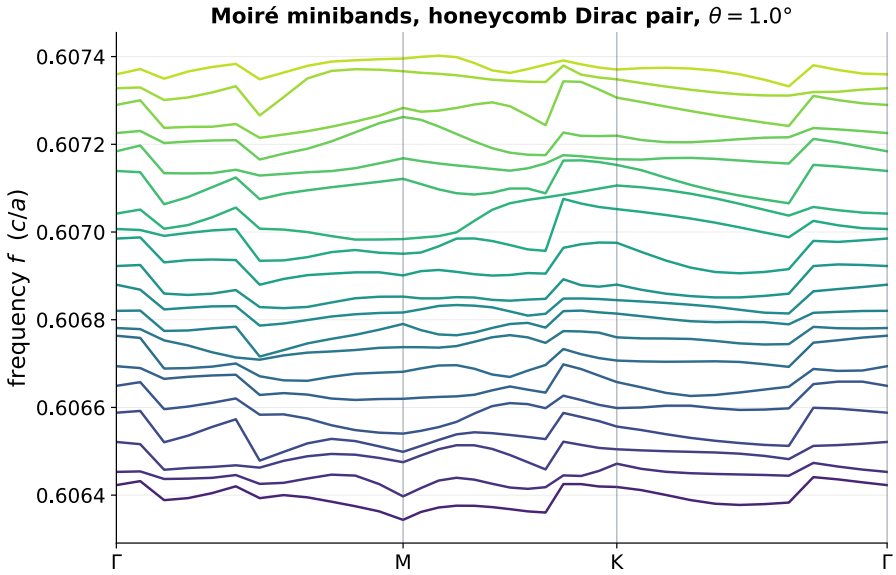

Figure 21: Moiré minibands of the honeycomb TM Dirac pair at $\theta = 1°$ along Γ–M–K–Γ of the moiré Brillouin zone, twelve points per segment, the twenty eigenvalues nearest the Dirac energy. Each curve is one miniband.

References

[1] R. Bistritzer and A. H. MacDonald. "Moiré bands in twisted double-layer graphene". In: *Proceedings of the National Academy of Sciences* 108.30 (2011), pp. 12233–12237. DOI: 10.1073/pnas.1108174108.

[2] Y. Cao, V. Fatemi, A. Demir, S. Fang, S. L. Tomarken, J. Y. Luo, J. D. Sanchez-Yamagishi, K. Watanabe, T. Taniguchi, E. Kaxiras, R. C. Ashoori, and P. Jarillo-Herrero. "Correlated insulator behaviour at half-filling in magic-angle graphene superlattices". In: *Nature* 556 (2018), pp. 80–84. DOI: 10.1038/nature26154.

[3] Y. Cao, V. Fatemi, S. Fang, K. Watanabe, T. Taniguchi, E. Kaxiras, and P. Jarillo-Herrero. "Unconventional superconductivity in magic-angle graphene superlattices". In: *Nature* 556 (2018), pp. 43–50. DOI: 10.1038/nature26160.

[4] J. D. Joannopoulos, S. G. Johnson, J. N. Winn, and R. D. Meade. *Photonic Crystals: Molding the Flow of Light*. 2nd ed. Princeton University Press, 2008. ISBN: 978-0-691-12456-8.

[5] P. Wang, Y. Zheng, X. Chen, C. Huang, Y. V. Kartashov, L. Torner, V. V. Konotop, and F. Ye. "Localization and delocalization of light in photonic moiré lattices". In: *Nature* 577 (2020), pp. 42–46. DOI: 10.1038/s41586-019-1851-6.

[6] H. Tang, F. Du, S. Carr, C. DeVault, O. Mello, and E. Mazur. "Modeling the optical properties of twisted bilayer photonic crystals". In: *Light: Science & Applications* 10 (2021), p. 157. DOI: 10.1038/s41377-021-00601-x.

[7] K. Dong, T. Zhang, J. Li, Q. Wang, F. Yang, Y. Rho, D. Wang, C. P. Grigoropoulos, J. Wu, and J. Yao. "Flat Bands in Magic-Angle Bilayer Photonic Crystals at Small Twists". In: *Physical Review Letters* 126 (2021), p. 223601. DOI: 10.1103/PhysRevLett.126.223601.

[8] B. Lou, N. Zhao, M. Minber, C. Guo, J. Vuckovic, and S. Fan. "Theory for Twisted Bilayer Photonic Crystal Slabs". In: *Physical Review Letters* 126 (2021), p. 136101. DOI: 10.1103/PhysRevLett.126.136101.

[9] X.-R. Mao, Z.-K. Shao, H.-Y. Luan, S.-L. Wang, and R.-M. Ma. "Magic-angle lasers in nanostructured moiré superlattice". In: *Nature Nanotechnology* 16 (2021), pp. 1099–1105. DOI: 10.1038/s41565-021-00956-7.

[10] C.-H. Yi, H. C. Park, and M. J. Park. "Strong interlayer coupling and stable topological flat bands in twisted bilayer photonic Moiré superlattices". In: *Light: Science & Applications* 11 (2022), p. 289. DOI: 10.1038/s41377-022-00977-4.

[11] L. Huang, W. Zhang, and X. Zhang. "Moiré Quasibound States in the Continuum". In: *Physical Review Letters* 128 (2022), p. 253901. DOI: 10.1103/PhysRevLett.128.253901.

[12] H. Qin, Z. Su, M. Liu, Y. Zeng, M.-C. Tang, M.-C. Li, Y. Deng, W. Zhou, J. Zhong, Q. Shi, et al. "Optical moiré bound states in the continuum". In: *Nature Communications* 15 (2024), p. 9080. DOI: 10.1038/s41467-024-53433-9.

[13] H. Tang, X. Ni, F. Du, V. Srikrishna, and E. Mazur. "Experimental probe of twist angle–dependent band structure of on-chip optical bilayer photonic crystal". In: *Science Advances* 9 (2023), eadh8498. DOI: 10.1126/sciadv.adh8498.

[14] Z. Yan, Y. Wang, X. Liu, et al. "Cavity quantum electrodynamics with moiré photonic crystal nanocavity". In: *Nature Communications* 16 (2025), p. 765. DOI: 10.1038/s41467-025-56107-w.

[15] M. Oudich, X. Kong, T. Zhang, C. Qiu, and Y. Jing. "Engineered Moiré Photonic and Phononic Superlattices". In: *Nature Materials* 23.9 (Aug. 2024), pp. 1169–1178. DOI: 10.1038/s41563-024-01950-9. URL: https://hal.science/hal-04795874.

[16] J. M. Luttinger and W. Kohn. "Motion of Electrons and Holes in Perturbed Periodic Fields". In: *Physical Review* 97.4 (1955), pp. 869–883. DOI: 10.1103/PhysRev.97.869.

[17] R. Winkler. *Spin-Orbit Coupling Effects in Two-Dimensional Electron and Hole Systems*. Vol. 191. Springer Tracts in Modern Physics. Berlin: Springer, 2003. DOI: 10.1007/b13586.

[18] M. V. Berry. "Quantal Phase Factors Accompanying Adiabatic Changes". In: *Proceedings of the Royal Society of London. Series A* 392.1802 (1984), pp. 45–57. DOI: 10.1098/rspa.1984.0023.

[19] F. Wilczek and A. Zee. "Appearance of Gauge Structure in Simple Dynamical Systems". In: *Physical Review Letters* 52.24 (1984), pp. 2111–2114. DOI: 10.1103/PhysRevLett.52.2111.

[20] P.-O. Löwdin. "A Note on the Quantum-Mechanical Perturbation Theory". In: *The Journal of Chemical Physics* 19.11 (1951), pp. 1396–1401. DOI: 10.1063/1.1748067.

[21] M. Born and K. Huang. *Dynamical Theory of Crystal Lattices*. Oxford University Press, 1954.

[22] R.-M. Lehner. *Website: Blaze2D Technical Report & Documentation*. GitHub Pages. 2026. URL: https://rnle.github.io/blaze2d/blaze/.

[23] S. G. Johnson and J. D. Joannopoulos. "Block-iterative frequency-domain methods for Maxwell's equations in a planewave basis". In: *Optics Express* 8.3 (2001), pp. 173–190. DOI: 10.1364/OE.8.000173.

[24] K. Yee. "Numerical solution of initial boundary value problems involving Maxwell's equations in isotropic media". In: *IEEE Transactions on Antennas and Propagation* 14.3 (1966), pp. 302–307. DOI: 10.1109/TAP.1966.1138693.

[25] A. Taflove and S. C. Hagness. *Computational Electrodynamics: The Finite-Difference Time-Domain Method*. 3rd ed. Artech House, 2005. ISBN: 978-1-58053-832-9.

[26] P. Yeh, A. Yariv, and C.-S. Hong. "Electromagnetic propagation in periodic stratified media. I. General theory". In: *Journal of the Optical Society of America* 67.4 (1977), pp. 423–438. DOI: 10.1364/JOSA.67.000423.

[27] A. Bensoussan, J.-L. Lions, and G. Papanicolaou. *Asymptotic Analysis for Periodic Structures*. North-Holland, 1978. ISBN: 978-0-444-85172-7.

[28] G. Allaire. "Homogenization and two-scale convergence". In: *SIAM Journal on Mathematical Analysis* 23.6 (1992), pp. 1482–1518. DOI: 10.1137/0523084.

[29] R.-M. Lehner. *Repository: Blaze2D - A Rust-based 2D PWE Maxwell Solver*. Open-source software. MIT License. 2026. URL: https://github.com/RnLe/blaze2d.

[30] R.-M. Lehner. *PyPI: blaze2d*. Version 0.5.1. Python package on PyPI. 2026. URL: https://pypi.org/project/blaze2d/.

[31] Y. Chen, T. A. Davis, W. W. Hager, and S. Rajamanickam. "Algorithm 887: CHOLMOD, Supernodal Sparse Cholesky Factorization and Update/Downdate". In: *ACM Transactions on Mathematical Software* 35.3 (2008), pp. 1–14. DOI: 10.1145/1391989.1391995.

[32] R.-M. Lehner. *Repository: MSL - Moire SuperLattice Generation and Analysis Pipeline*. Open-source software. 2026. URL: https://github.com/RnLe/msl.

[33] R.-M. Lehner. *Website: MSL Documentation*. GitHub Pages. 2026. URL: https://rnle.github.io/msl/.